

1 **Fast odour dynamics are encoded in the olfactory system and guide behaviour**

2  
3 Tobias Ackels<sup>1,2,3</sup>, Andrew Erskine<sup>1,2,3</sup>, Debanjan Dasgupta<sup>1,2,3</sup>, Alina Cristina Marin<sup>1</sup>,  
4 Tom P.A. Warner<sup>1</sup>, Sina Tootoonian<sup>1,2</sup>, Izumi Fukunaga<sup>1</sup>, Julia J. Harris<sup>1,2</sup> and Andreas T.  
5 Schaefer<sup>1,2\*</sup>

6  
7 <sup>1</sup>The Francis Crick Institute, Neurophysiology of Behaviour Laboratory, London, UK

8 <sup>2</sup>Department of Neuroscience, Physiology & Pharmacology, University College London, UK

9 <sup>3</sup>These authors contributed equally

10 \*Correspondence should be addressed to andreas.schaefer@crick.ac.uk

11 **Abstract**

12 **Odours are transported in turbulent plumes resulting in rapid concentration**  
13 **fluctuations<sup>1,2</sup> that contain rich information about the olfactory scenery, such as**  
14 **odour source composition and location<sup>2-4</sup>. Yet whether the mammalian olfactory**  
15 **system has access to the underlying temporal structure to extract information**  
16 **about the environment remains unknown. Here, we show that 10 ms odour pulse**  
17 **patterns result in distinct responses in olfactory receptor neurons. In operant**  
18 **conditioning experiments mice discriminated temporal correlations of rapidly**  
19 **fluctuating odours at frequencies of up to 40 Hz. In imaging and**  
20 **electrophysiological recordings, such correlation information could be readily**  
21 **extracted from the activity of mitral and tufted cells, the output of the olfactory**  
22 **bulb. Furthermore, we show that temporal correlation of odour concentrations<sup>5</sup>**  
23 **reliably predicts whether odorants emerge from the same or different sources in**  
24 **naturalistic environments with complex airflow. Training mice on such tasks and**  
25 **probing with synthetic correlated stimuli at different frequencies suggests that**  
26 **mice can indeed use the temporal structure of odours to extract information about**  
27 **space. Our work thus demonstrates that the mammalian olfactory system has**  
28 **access to unexpectedly fast temporal features in odour stimuli. This in turn endows**  
29 **animals with the capacity to overcome key behavioural challenges such as odour**  
30 **source separation<sup>5</sup>, figure-ground segregation<sup>6</sup> and odour localisation<sup>7</sup>, by**  
31 **extracting information about space from temporal odour dynamics.**

32 **Main text**

33 The turbulent nature of air<sup>1,2,4,8</sup> as well as water<sup>9,10</sup> flow results in complex temporal  
34 fluctuations of odour concentrations that depend on the distance and direction of odour  
35 sources<sup>1-4,8,10</sup>. Insects are thought to use the temporal structure of odour plumes to infer  
36 e.g. odour source location<sup>4,7,11-13</sup> or composition<sup>13-15</sup>. Mammalian olfaction on the other  
37 hand has generally been considered a slow sense. Individual sniffs are thought to be the  
38 unit of information<sup>16</sup>, implying that fast odour concentration changes (at sub-sniff  
39 resolution) should be inaccessible to the mammalian olfactory system. However, the  
40 neural circuitry of e.g. the mouse olfactory bulb (OB) is in principle capable of

41 millisecond-precise action potential firing<sup>17,18</sup>, and is endowed with rich computational  
42 resources that could be employed to extract fine temporal information from dynamic  
43 inputs<sup>19</sup>. Here, we show that the mouse olfactory system has access to fast, sub-sniff  
44 temporal patterns in the odour scenery and that mice can use this information to detect  
45 high-frequency odour correlations enabling source separation.

#### 46 **Fast odour dynamics encoded in OB inputs**

47 Normal airflow is characterized by complex, often turbulent, flow patterns and imposes  
48 a rich temporal structure on odour concentration profiles with significant power in  
49 frequencies well above typical sniff rates (**Fig. 1a**). To assess whether the mouse olfactory  
50 system has access to this frequency regime, we designed an odour delivery system  
51 capable of reliably presenting odours with a bandwidth beyond 50 Hz (**Fig. 1b**,  
52 **Supplementary Methods Fig. 1**). As prototypical, simplistic high frequency stimuli we  
53 employed two 10 ms square pulses of odour separated by 10 or 25 ms (**Fig. 1c**). Olfactory  
54 sensory neurons (OSN) are known to be slow in responding to odour stimuli<sup>20</sup>. Both  
55 epithelial mucus and the biochemical transduction cascade act as low-pass filters<sup>16,20,21</sup>,  
56 suggesting that individual OSNs cannot directly follow rapidly fluctuating odour stimuli.  
57 However, axons from up to 10s of thousands of OSNs that express the same olfactory  
58 receptor converge onto one or a few glomeruli in the OB<sup>22</sup>. This organization resembles  
59 the auditory system where, despite the relatively low temporal resolution of individual  
60 cells, population responses faithfully report high-frequency signals<sup>23</sup>. Thus, we built a  
61 model of populations of noisy integrate-and-fire neurons with stimulus filtering and  
62 neuronal dynamics matching experimental data to explore whether this large  
63 convergence could aid in detecting high frequency stimuli in OSNs (**Extended Data Fig.**  
64 **1**). Our simulation results suggest that across the thousands of OSNs that express the  
65 same OR – while still not directly following the odour profile – the population can  
66 faithfully discriminate between such 10/25 ms stimulation (**Extended Data Fig. 1d,f,h**).  
67 Key high-frequency information in the odour profile might, therefore, be preserved in the  
68 inputs to the OB.

69 To test this experimentally, we performed  $\text{Ca}^{2+}$  imaging experiments in anaesthetized and  
70 awake mice expressing GCaMP6f in OSNs (**Fig. 1c-i**, **Extended Data Fig. 2**) whilst  
71 delivering odour pulses locked to inhalation (**Fig. 1c,d**). Overall, responses for all  
72 glomeruli were highly correlated between the two stimuli (**Fig. 1f,g**). Glomerular activity  
73 did not directly follow the 10ms or 25 ms pulses (**Fig. 1f**). However, in 1/3 of glomeruli  
74 ( $n = 33/100$ ,  $p < 0.01$ ), responses were consistently and significantly different for the two  
75 stimuli (**Fig. 1f-h**, **Extended Data Fig. 2**) mirroring the simulation results (**Extended**  
76 **Data Fig. 1**). Notably, just a few dozen randomly chosen glomeruli were sufficient to  
77 discern between the stimuli at >80% success rate with a linear classifier (**Fig. 1i**, see also  
78 **Extended Data Fig. 1h**). Expanding the stimulus set to different concentrations and  
79 multiple pulses (**Extended Data Fig. 2**) confirmed that information about concentration  
80 and temporal patterns with features exceeding the 25 ms timescale is reliably and  
81 independently preserved in the population of OSNs.

82 **Discrimination of correlation structure**

83 Can mice base behaviour on such high frequency stimuli? We trained mice in an  
84 automated go/no-go operant conditioning system ("AutonoMouse"<sup>24</sup>, **Fig. 2a**,  
85 **Supplementary Video 1**) to discriminate between high frequency stimuli. To ascertain  
86 that the brief odour pulses were delivered during inhalation in freely moving mice we  
87 opted for 2 second pulse trains at different frequencies with constant airflow (**Fig. 2b**).  
88 We found that mice can discriminate whether an odour is presented at e.g. 4 Hz or 20 Hz,  
89 yet the apparent "critical flicker frequency" (**Fig. 2c, Extended Data Fig. 3**) was  
90 significantly lower than frequencies OSNs readily represent (**Fig. 1, Extended Data Fig.**  
91 **1,2**). However, in both visual and auditory systems, conventional flicker fusion frequency  
92 or gap detection thresholds substantially underestimate the temporal sensitivity,  
93 particularly for tasks with multiple stimuli present<sup>23,25,26</sup>: In vision, for example, flicker  
94 fusion frequency is around 60 Hz, whereas thresholds for detecting synchrony between  
95 stimuli has been reported to be 3 ms<sup>26</sup>. Thus, we wanted to probe whether, similarly,  
96 olfactory tasks involving multiple odours reveal behavioural access to higher frequencies.  
97 We presented stimuli composed of two odours fluctuating in a correlated or anti-  
98 correlated manner as the rewarded and unrewarded stimulus, respectively (and vice  
99 versa, **Fig. 2d-f**). Mice readily learned to differentially respond to correlated or anti-  
100 correlated odours (**Fig. 2h-k**). Gradually increasing the correlation frequency showed  
101 that animals were capable of reliably detecting the correlation structure of stimuli at  
102 frequencies of up to 40 Hz (**Fig. 2h,j,k**). As a population, animal performance decreased  
103 by approximately 5% per octave with performance significantly above chance at  
104 frequencies of up to 40 Hz (n = 33 mice in two cohorts of 14 and 19 mice, **Fig. 2k**). To  
105 mitigate the risk of animals using non-intended cues for discrimination, odours were  
106 presented from changing valve combinations (**Fig. 2g, Extended Data Fig. 4**), odour flow  
107 was carefully calibrated (**Fig. 2e, Extended Data Fig. 4d-e**) and additionally varied  
108 randomly between trials such that neither flow nor valve clicking noises or average  
109 concentration provided any information about the nature of the stimulus (**Extended**  
110 **Data Fig. 4d-h**). Consistent with this, when valve identities were scrambled, animals  
111 performed at chance (grey, **Fig. 2k**). Finally, when odour presentation was changed to a  
112 new set of valves, performance levels were maintained (**Fig. 2g-i and Extended Data Fig.**  
113 **4i-k**), indicating that only intended cues (the temporal structure of odours) were used  
114 for discrimination. Performance was independent of the odour pair used (**Extended Data**  
115 **Fig. 3g**) and maintained for tasks discriminating correlated from uncorrelated (rather  
116 than anti-correlated) odours (**Extended Data Fig. 3e,f**).

117 Mice tended to take more time to detect the correlation structure of stimuli with higher  
118 fluctuation frequencies (**Extended Data Fig. 5j-l**). This was most pronounced for animals  
119 with higher overall performance (**Extended Data Fig. 5j**). Accuracy strongly correlated  
120 with reaction time across all stimuli and animals (**Extended Data Fig. 5k**) despite the  
121 fact that total time of odour delivery was the same across all trials regardless of stimulus  
122 frequency. Consequently, when analysis was restricted to trials where mice sampled the  
123 stimuli long enough, e.g. for at least 750 ms, performance significantly increased across

124 frequencies ([Extended Data Fig. 5l](#)). This indicates that the measured performance  
125 might not be the psychophysical limit for discriminating fluctuating odour stimuli.  
126 Furthermore, this suggests that mice integrate information across large portions of the  
127 presented stimuli, rather than e.g. detecting simultaneity of odour onset<sup>14</sup> to determine  
128 whether odours were correlated or not. To directly test this possible strategy, we  
129 interleaved training trials with probe trials where the onset characteristics were flipped  
130 ([Extended Data Fig. 5f-i](#)). Notably, performance did not drop substantially ([Extended](#)  
131 [Data Fig. 5h,i](#)), consistent with a strategy that relies primarily on discerning the high  
132 frequency correlation structure of the stimulus over several 100 ms rather than the onset  
133 only ([Extended Data Fig. 5f,g,i](#)). Sniff rate in turn was independent of the correlation  
134 frequency of stimuli presented ([Extended Data Fig. 5a-e](#)).

### 135 **Odour correlation encoded in OB output**

136 To assess how this high-frequency information is represented and reformatted in the  
137 olfactory system, we imaged neural activity in response to high-frequency stimuli ([Fig.](#)  
138 [3](#)).  $\text{Ca}^{2+}$  imaging of OSN responses to correlated and anti-correlated stimuli showed that  
139 – unlike for two pulses with variable gaps ([Fig. 1](#)) – correlation structure of odour pulse  
140 trains was difficult to discern on the level of inputs to the OB using simple linear  
141 classifiers ([Extended Data Fig. 6](#)). Directly imaging from the *output* of the OB, mitral and  
142 tufted cells (M/TCs, [Fig. 3a-g](#), [Extended Data Fig. 7](#)), showed that overall, M/TCs also  
143 responded similarly to correlated and anti-correlated stimuli ([Extended Data Fig. 7j-l](#)).  
144 17% of all M/TCs, however, showed significantly different integral responses (0-5 sec  
145 after odour onset,  $p < 0.01$ ) to the two stimuli (114/680 ROIs, [Fig. 3d-f](#)). As a result,  
146 correlated and anti-correlated odours were reliably discriminated by a linear classifier  
147 using the M/TC population responses (somatic response [Fig. 3g](#), dendritic response  
148 [Extended Data Fig. 7d,i](#)) unlike for the OSN population response ([Extended Data Fig.](#)  
149 [6k,l](#)). This is consistent with the idea that the OB circuitry implements a non-linear  
150 transformation of OSN input where the representation of correlation becomes more  
151 readily accessible in the OB output.

152 We employed odour stimuli rapidly fluctuating at frequencies that substantially exceeded  
153 the temporal resolution of  $\text{Ca}^{2+}$  imaging, which captures a low-pass filtered signal of  
154 neural activity. Although the  $\text{Ca}^{2+}$  signal does not follow individual stimulus frequencies,  
155 the M/TC population response contained enough information to determine whether a  
156 correlated or anti-correlated stimulus was presented. To probe whether additional  
157 information about stimuli is present in the output of the OB at finer time scales, we turned  
158 to extracellular unit recordings ([Fig. 3h-k](#), [Extended Data Fig. 8](#)) and whole-cell patch  
159 recordings ([Extended Data Fig. 9](#)). Despite the kHz temporal resolution, single-units also  
160 did not directly follow high-frequency stimuli. Average activity (summed spike count  
161 during 500 ms after odour onset) was, however, significantly different between  
162 correlated and anti-correlated stimuli in 24% of single-units (23/97,  $p < 0.01$ , Mann-  
163 Whitney U test, [Fig. 3i,j](#), [Extended Data Fig. 8b](#)), consistent with the  $\text{Ca}^{2+}$  imaging results.  
164 As few as 60 randomly selected units were sufficient to classify the odour stimuli with

165 >80% accuracy (**Fig. 3k**). Additional information was contained at finer time scales as  
166 increasing the temporal resolution of analysis improved discriminability (**Fig. 3k and**  
167 **Extended Data Fig. 8e-g**). Together, these results demonstrate that information about  
168 high-frequency correlation structure in odours is accessible to the animal for behavioural  
169 decisions and readily available in the output of the OB.

170 **Correlations allow for source separation**

171 What could the detection of high-frequency correlations be useful for? Natural odours  
172 consist of multiple different types of molecules, and a typical olfactory scene contains  
173 several sources<sup>6</sup>. To make sense of the olfactory environment, the brain must be able to  
174 separate odour sources, attributing the various chemicals present to the same or different  
175 objects<sup>5</sup>. Motivated by the turbulent nature of odour transport, Hopfield suggested that  
176 the temporal structure of odour concentration fluctuations might contain location  
177 information about odour sources<sup>5</sup> - i.e. that chemicals belonging to the same source  
178 would co-fluctuate in concentration. Detecting correlations in odour fluctuations would  
179 thus allow mice to discern which odours arise from the same object. To experimentally  
180 probe the potential of odour correlation structure to facilitate odour source separation in  
181 air, we devised a dual-energy fast photoionisation detection method to simultaneously  
182 measure the odour concentrations of two odours with high temporal bandwidth  
183 (Methods, **Fig. 4a,b**, **Extended Data Fig. 10a-e** and **Supplementary Methods Fig. 2**).  
184 When an odour was presented in a laboratory environment with artificially generated  
185 complex airflow patterns (**Fig. 4a**), to mimic the outdoor measurements (**Fig. 1a**), odour  
186 concentration fluctuated with a spectrum extending beyond 40 Hz (**Extended Data Fig.**  
187 **10a**). When two odours were presented from the same source, these fluctuations were  
188 highly correlated (**Fig. 4a,b** and **Extended Data Fig. 10b**). When we separated odour  
189 sources and presented the two odours 50 cm apart, odour dynamics were uncorrelated  
190 (**Fig. 4a,b**) with intermediate correlations for closer distances (**Fig. 4b**). This pattern of  
191 almost perfect correlation for the same source and virtually uncorrelated dynamics for  
192 separated sources was maintained at closer and farther distances between odour source  
193 and sensor (**Extended Data Fig. 10d**), independent of the odours used (**Extended Data**  
194 **Fig. 10c**) and was mirrored outdoors (**Extended Data Fig. 10e**). Thus, the correlation  
195 structure of odorant concentration fluctuations indeed contains reliable information  
196 about odour objects – e.g. whether odours emerge from the same or different sources.

197 Can mice make use of this information? We trained a new cohort of mice in a modified  
198 AutonoMouse setting, presenting odours corresponding to the “same source” or “source  
199 separated” case as rewarded or unrewarded stimuli (**Fig. 4c,d** and **Extended Data Fig.**  
200 **10**). Mice were able to learn to discriminate these stimuli (**Fig. 4d,e**). Once the task was  
201 acquired, we probed their performance with artificially generated stimuli (**Extended**  
202 **Data Fig. 10f-k**) that were derived from prior measurements with natural airflow but  
203 perfectly correlated (**Fig. 4e**). Notably, they reliably responded to these probe trials with  
204 correlated stimuli as they did to the “same source” stimuli they had been trained on (**Fig.**  
205 **4e, Extended Data Fig. 10m**). To further ascertain that they were using the correlation

206 structure to make these decisions, we probed with artificial square pulse stimuli (as in  
207 **Fig. 2, 3**) at different frequencies. Mice performed significantly above chance in probe  
208 trials at frequencies of up to 40 Hz (**Fig. 4e, Extended Data Fig. 10s**), implying that  
209 learning about source separation directly translates to distinguishing temporal features  
210 in correlated / uncorrelated stimuli.

211 **Discussion**

212 Here, we have shown that the mammalian olfactory system has access to temporal  
213 features of odour stimuli at frequencies of at least up to 40 Hz. We have demonstrated  
214 access to information in rapid odour fluctuations using different behavioural  
215 experiments (**Fig. 2,4**). We have shown reliable decoding from imaging and unit  
216 recordings from different stages of the olfactory system using both correlated odour  
217 concentration fluctuations (**Fig. 3, Extended Data Fig. 7, 8a-g**) as well as simplistic  
218 paired pulse stimuli with gaps as small as 25 ms (**Fig. 1, Extended Data Fig. 2, 8h-l**),  
219 corroborated by computational modelling (**Extended Data Fig. 1**). Our results are  
220 consistent with recent findings that the olfactory bulb circuitry not only enables highly  
221 precise odour responses<sup>17,18</sup> but enables detection of optogenetically evoked inputs with  
222 a precision of 10-30 ms<sup>27-29</sup> with different projection neurons displaying distinct firing  
223 patterns in response to optogenetic stimulation<sup>29</sup>. While behavioural and physiological  
224 responses to precisely timed odour stimuli have been observed in insects<sup>13,15,30</sup>, in  
225 mammals the complex shape of the nasal cavity was generally thought to low-pass filter  
226 any temporal structure of the incoming odour plume. Our results show that while the  
227 low-pass filtering in the nose and by OSNs might reduce the ability of neurons to directly  
228 follow high-frequency stimuli, sufficient information about high-frequency content is  
229 preserved and available such that mice can readily make use of this information.

230 What could such high bandwidth be useful for? We have shown that odour sources even  
231 in close proximity differ in their temporal correlation structure. Thus, the ability to detect  
232 whether odorants are temporally correlated could allow mice to perform source  
233 separation, solving the "olfactory cocktail party problem"<sup>5,6</sup> without prior knowledge  
234 about the odour scenery. We show that mice can indeed discriminate between "one  
235 source / separated source" stimuli. They readily translate this discrimination to artificial  
236 correlated pulse trains demonstrating that they are using correlation structure to make  
237 this distinction. Distinguishing between other environmental features, such as distance  
238 or direction of an odour source, could also be achieved by extracting temporal features  
239 from odour fluctuations<sup>1-3,8</sup> possibly in combination with strategies comparing  
240 information reaching the brain through the two nares<sup>31,32</sup>.

241 How exactly is this temporal information extracted? While insects are able to detect the  
242 simultaneity of onset of two odours<sup>14,33,34</sup>, this strategy is unlikely to be the dominant  
243 means that mice use to detect correlation (**Extended Data Fig. 5**). Similarly, mice do not  
244 show adjustment of sniff strategies for discriminating high frequency odour correlations  
245 (**Extended Data Fig. 5, Supplementary Video 2**). While individual mammalian OSNs are  
246 thought to be quite slow and unreliable<sup>20</sup>, the large convergence of OSN axons provides a

247 substrate to create the needed high temporal bandwidth<sup>35</sup> ([Extended Data Fig. 1](#)).  
248 Biophysical heterogeneity of OSNs might improve how the population encodes  
249 temporally structured stimuli<sup>36,37</sup>. Intrinsic cellular biophysics ([Extended Data Fig. 9](#)),  
250 local interneurons or long-range lateral inhibition<sup>5,38</sup> might permit the extraction of  
251 temporal correlation within the olfactory bulb circuitry and possibly result in individual  
252 projection neurons tuned to specific temporal structures.

253 The turbulence of odour plumes has often been viewed as a source of noise for mammals.  
254 In contrast, we find that the mouse olfactory system has access to high-frequency  
255 temporal features in odour stimuli. This opens up a new perspective on how mice could  
256 make use of natural turbulence in order to obtain information about their spatial  
257 environment. This in turn provides new computational challenges for the mammalian  
258 olfactory system and an entry point into how information about space is extracted from  
259 sensory inputs.

260 **References**

- 261 1. Fackrell, J. & Robins, A. Concentration fluctuations and fluxes in plumes from  
262 point sources in a turbulent boundary layer. *J. Fluid Mech.* **117**, 1–26 (1982).
- 263 2. Mylne, K. R. & Mason, P. J. Concentration fluctuation measurements in a  
264 dispersing plume at a range of up to 1000 m. *Q. J. R. Meteorol. Soc.* **117**, 177–206  
265 (1991).
- 266 3. Schmuker, M., Bahr, V. & Huerta, R. Exploiting plume structure to decode gas  
267 source distance using metal-oxide gas sensors. *Sensors Actuators B Chem.* **235**,  
268 636–646 (2016).
- 269 4. Murlis, J., Elkington, J. S. & Carde, R. T. Odor Plumes And How Insects Use Them.  
270 *Annu. Rev. Entomol.* **37**, 505–532 (1992).
- 271 5. Hopfield, J. J. Olfactory computation and object perception. *PNAS* **88**, 6462–6  
272 (1991).
- 273 6. Rokni, D., Hemmeler, V., Kapoor, V. & Murthy, V. N. An olfactory cocktail party:  
274 figure-ground segregation of odorants in rodents. *Nat. Neurosci.* **17**, 1225–1232  
275 (2014).
- 276 7. Vergassola, M., Villermaux, E. & Shraiman, B. I. ‘Infotaxis’ as a strategy for  
277 searching without gradients. *Nature* **445**, 406–409 (2007).
- 278 8. Celani, A., Villermaux, E. & Vergassola, M. Odor Landscapes in Turbulent  
279 Environments. *Phys. Rev. X* **4**, 041015 (2014).
- 280 9. Crimaldi, J. P. & Koseff, J. R. High-resolution measurements of the spatial and  
281 temporal scalar structure of a turbulent plume. *Exp. Fluids* **31**, 90–102 (2001).
- 282 10. Moore, P. A. & Atema, J. Spatial Information in the Three-Dimensional Fine  
283 Structure of an Aquatic Odor Plume. *Biol. Bull.* **181**, 408–418 (1991).

284 11. Mafra-Neto, A. & Cardé, R. T. Fine-scale structure of pheromone plumes  
285 modulates upwind orientation of flying moths. *Nature* **369**, 142–144 (1994).

286 12. Vickers, N. J. Mechanisms of animal navigation in odor plumes. *Biol. Bull.* **198**,  
287 203–212 (2000).

288 13. Riffell, J. A., Sanders, E., *et al.* Flower discrimination by pollinators in a dynamic  
289 chemical environment. *Science* **344**, 1515–1518 (2014).

290 14. Szyszka, P., Stierle, J. S., Biergans, S. & Galizia, C. G. The speed of smell: Odor-object  
291 segregation within milliseconds. *PLoS One* **7**, 4–7 (2012).

292 15. Szyszka, P., Gerkin, R. C., Galizia, C. G. & Smith, B. H. High-speed odor transduction  
293 and pulse tracking by insect olfactory receptor neurons. *Proc. Natl. Acad. Sci.* **111**,  
294 16925–16930 (2014).

295 16. Kepcs, A., Uchida, N. & Mainen, Z. F. The sniff as a unit of olfactory processing.  
296 *Chem. Senses* **31**, 167–179 (2006).

297 17. Shusterman, R., Smear, M. C., Koulakov, A. A. & Rinberg, D. Precise olfactory  
298 responses tile the sniff cycle. *Nat. Neurosci.* **14**, 1039–44 (2011).

299 18. Cury, K. M. & Uchida, N. Robust Odor Coding via Inhalation-Coupled Transient  
300 Activity in the Mammalian Olfactory Bulb. *Neuron* **68**, 570–585 (2010).

301 19. Burton, S. D. Inhibitory circuits of the mammalian main olfactory bulb. *J.  
302 Neurophysiol.* **84** 112, (2017).

303 20. Duchamp-Viret, P., Chaput, M. A. & Duchamp, A. Odor Response Properties of Rat  
304 Olfactory Receptor Neurons. *Science* **284**, 2171–2174 (1999).

305 21. Munger, S. D., Leinders-Zufall, T. & Zufall, F. Subsystem organization of the  
306 mammalian sense of smell. *Annu. Rev. Physiol.* **71**, 115–40 (2009).

307 22. Bressel, O. C., Khan, M. & Mombaerts, P. Linear correlation between the number of  
308 olfactory sensory neurons expressing a given mouse odorant receptor gene and  
309 the total volume of the corresponding glomeruli in the olfactory bulb. *J. Comp.  
310 Neurol.* **524**, 199–209 (2016).

311 23. Carr, C. E. & Amagai, S. Processing of temporal information in the brain. *Adv.  
312 Psychol.* **115**, 27–52 (1996).

313 24. Erskine, A., Bus, T., Herb, J. T. & Schaefer, A. T. AutonoMouse: High throughput  
314 automated operant conditioning shows progressive behavioural impairment with  
315 graded olfactory bulb lesions. *PLoS One* 291815 (2019)  
316 doi:<https://doi.org/10.1371/journal.pone.0211571>.

317 25. Brown, J. L. Visual Sensitivity. *Annu. Rev. Psychol.* **24**, 151–186 (1973).

318 26. Westheimer, G. & McKee, S. P. Perception of temporal order in adjacent visual  
319 stimuli. *Vision Res.* **17**, 887–892 (1977).

320 27. Smear, M., Shusterman, R., O'Connor, R., Bozza, T. & Rinberg, D. Perception of sniff  
321 phase in mouse olfaction. *Nature* **479**, 397–400 (2011).

322 28. Rebello, M. R., McTavish, T. S., *et al.* Perception of Odors Linked to Precise Timing  
323 in the Olfactory System. *PLoS Biol.* **12**, (2014).

324 29. Li, A., Gire, D. H., Bozza, T. & Restrepo, D. Precise Detection of Direct Glomerular  
325 Input Duration by the Olfactory Bulb. *J. Neurosci.* **34**, 16058–16064 (2014).

326 30. Geffen, M. N., Broome, B. M., Laurent, G. & Meister, M. Neural encoding of rapidly  
327 fluctuating odors. *Neuron* **61**, 570–86 (2009).

328 31. Rajan, R., Clement, J. & Bhalla, U. Rats Smell in Stereo. *Science* **311**, 666–670  
329 (2006).

330 32. Catania, K. C. Stereo and serial sniffing guide navigation to an odour source in a  
331 mammal. *Nat. Commun.* **4**, 1441 (2013).

332 33. Baker, T., Fadamiro, H. & Cosse, A. Moth uses fine tuning for odour resolution.  
333 *Nature* **393**, 530 (1998).

334 34. Stierle, J. S., Galizia, C. G. & Szyszka, P. Millisecond stimulus onset-asynchrony  
335 enhances information about components in an odor mixture. *J. Neurosci.* **33**,  
336 6060–9 (2013).

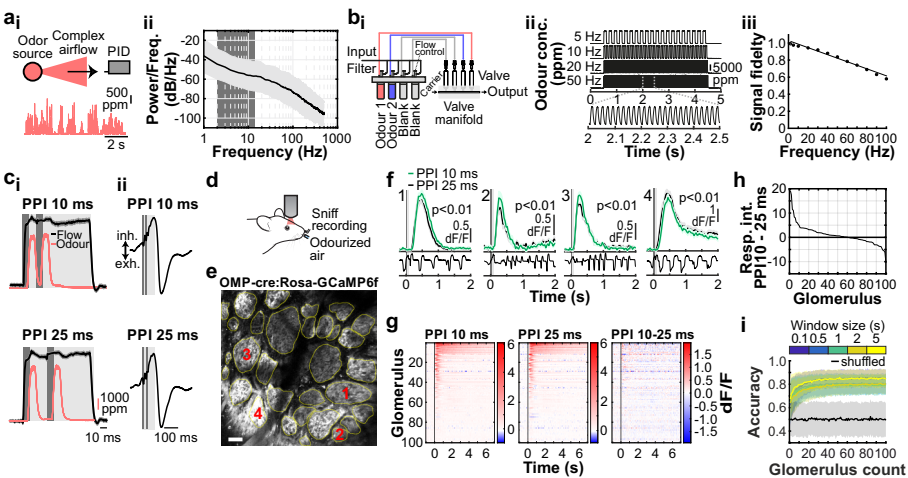
337 35. Abeles, M. Time Is Precious. *Science* **304**, 523–524 (2004).

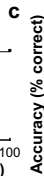
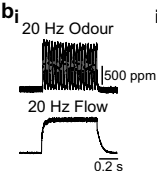
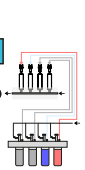
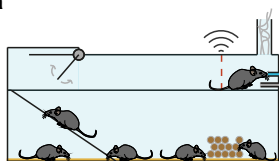
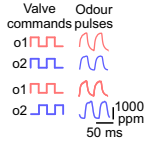
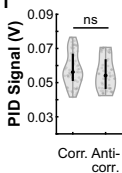
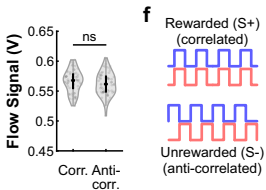
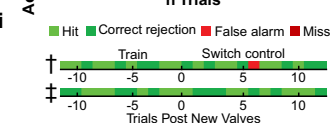
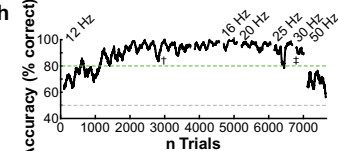
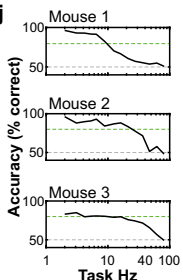
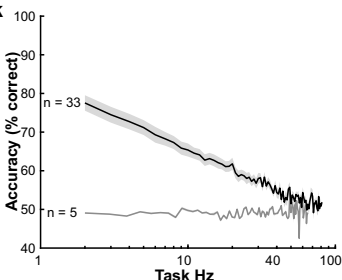
338 36. Padmanabhan, K. & Urban, N. N. Intrinsic biophysical diversity decorrelates  
339 neuronal firing while increasing information content. *Nat. Neurosci.* **13**, 1276–82  
340 (2010).

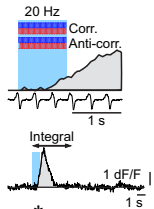
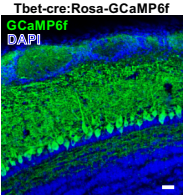
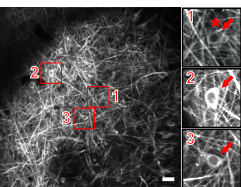
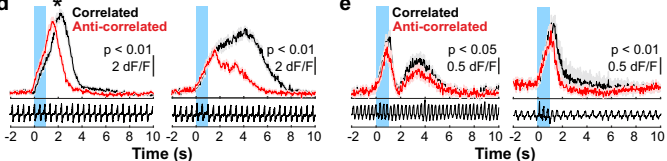
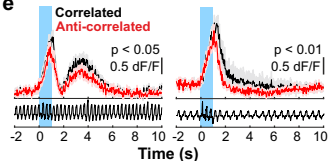
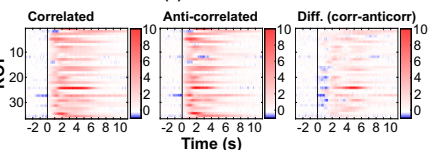
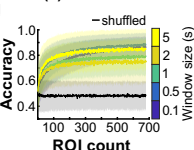
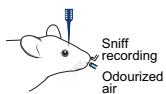
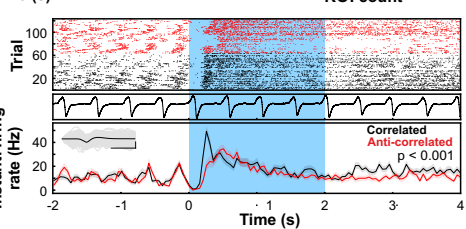
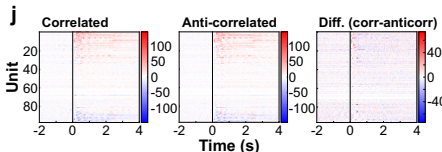
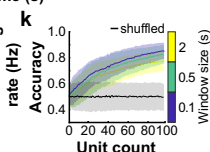
341 37. Park, I. M., Bobkov, Y. V., Ache, B. W. & Príncipe, J. C. Intermittency Coding in the  
342 Primary Olfactory System: A Neural Substrate for Olfactory Scene Analysis. *J.*  
343 *Neurosci.* **34**, 941–952 (2014).

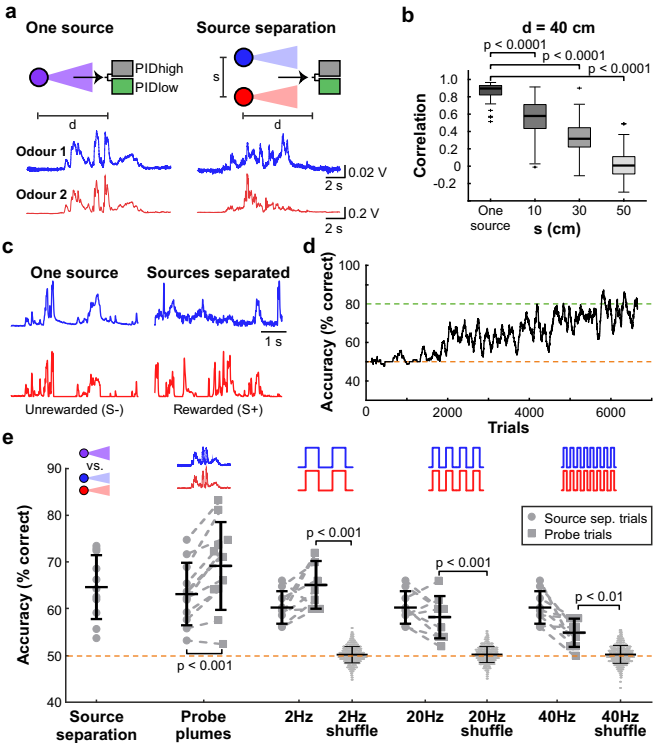
344 38. Fukunaga, I., Herb, J. T., Kollo, M., Boyden, E. S. & Schaefer, A. T. Independent  
345 control of gamma and theta activity by distinct interneuron networks in the  
346 olfactory bulb. *Nat. Neurosci.* **17**, 1208–1216 (2014).

347



**a****d****e****ii****h****j****k**

**a****b****c****d****e****f****g****h****i****j****k**



348 **Fig. 1 | Sub-sniff detection of odour signals in olfactory bulb inputs.**  
349 **a<sub>i</sub>**, Example odour plume recorded outdoors under natural, complex airflow conditions  
350 using a photoionisation detector (PID). **a<sub>ii</sub>**, Averaged power spectrum of all recorded  
351 odour plumes (n=37 plumes, mean±SD of log power), typical range of sniff frequencies  
352 observed in mice highlighted in dark grey. **b<sub>i</sub>**, Schematic of multi-channel high bandwidth  
353 odour delivery device. **b<sub>ii</sub>**, Representative odour pulse recordings at command  
354 frequencies between 5 and 50Hz. **b<sub>iii</sub>**, Relationship of frequency and odour pulse signal  
355 fidelity (see Methods, n=5 repeats for each frequency, mean±SEM, see also  
356 **Supplementary Methods Fig. 1**). **c<sub>i</sub>**, Odour (red) and flow traces (black) of 10ms paired  
357 pulse interval (PPI) stimuli for 10ms (top) and 25ms (bottom), valve commands are  
358 shown in dark grey. **c<sub>ii</sub>**, Stimuli are presented during the inhalation phase of the  
359 respiration cycle. **d**, Schematic of the two-photon imaging approach. **e**, GCaMP6f  
360 fluorescence recorded in olfactory bulb glomeruli (maximum projection of 8200 frames,  
361 marked glomeruli correspond to example traces shown in **f**). Scale bar: 50µm. **f**, Example  
362 calcium traces in response to 10 and 25ms PPI odour stimuli (mean of 10 trials±SEM,  
363 unpaired two-sided t-test for 2s response-integral from odour onset). Bottom: Example  
364 respiration trace. **g**, Calcium transients as colour maps for PPI 10ms (left), PPI 25ms  
365 (middle), and the difference between both odour stimulations (right). Glomeruli are  
366 sorted by response magnitude to the PPI 10ms stimulus. **h**, Glomerular responses sorted  
367 by magnitude of difference to PPI 10 vs. 25ms. **i**, Classifier accuracy over all glomeruli  
368 when a linear classifier was trained on several response windows (colour-coded, black:  
369 shuffle control) to PPI 10 vs. 25ms stimuli (n=up to 100 glomeruli from 5 individual  
370 animals; mean±SD of 500 repetitions). Throughout, ethyl butyrate was used as the odour  
371 stimulus.

372 **Fig. 2 | Mice can discriminate odour correlation structure at frequencies up to**  
373 **40Hz.** **a**, Schematic of the automated operant conditioning system (“AutonoMouse”)  
374 housing cohorts of up to 25 animals. **b<sub>i</sub>**, Representative trace of a 20Hz odour pulse train  
375 (top) and corresponding stable airflow (bottom). **b<sub>ii</sub>**, Relationship of frequency and total  
376 amount of odour released (n=5 repeats for each frequency, mean±SEM). **c**, Group  
377 accuracy in frequency discrimination task (n=10 mice, p<0.001 for all stimuli compared  
378 to chance accuracy (paired two-sided t-test); see also **Extended Data Fig. 3**). Boxes  
379 indicate 25<sup>th</sup>–75<sup>th</sup> percentiles, thick line is median, whiskers are most extreme data points  
380 not considered outliers, see Methods. **d**, Left: Valve commands to release two odours  
381 fluctuating at 20 Hz in a correlated (top) or anti-correlated (bottom) manner. Right:  
382 Resultant odour concentration changes measured using dual-energy photoionisation  
383 detectors (**Supplementary Methods Fig. 2**). **e**, Odour (**e<sub>i</sub>**) and flow (**e<sub>ii</sub>**) signal for  
384 correlated and anti-correlated stimuli fluctuating at 20Hz (n=60 trials for each condition;  
385 odour: p=0.19, flow: p=0.23, unpaired two-sided t-test). Median shown as black dot, first  
386 and third quartile are bounds of the black bar. **f**, Schematic of the discrimination stimuli;  
387 mice were trained to discriminate between two odours presented simultaneously in  
388 either a correlated (top) or anti-correlated (bottom) fashion in a standard go/no-go  
389 paradigm. **g**, Schematic of valve combinations for stimulus production. Train: 6 valves are

390 used to produce the stimulus through varying valve combinations. Switch control: two  
391 extra valves are introduced and odour presentation switched over to the newly  
392 introduced valves. **h**, Example animal performing the correlation discrimination task at  
393 different frequencies. **i**, Trial response maps before and after switch to control valves (as  
394 described in **g**, n=12 trials pre-, n=12 trials post-new valve introduction). Symbols  
395 indicate time point of valve introduction as marked in **h**, see also [Extended Data Fig. 4](#).  
396 **j**, Accuracy of 3 representative animals performing correlation discrimination where  
397 stimulus pulse frequency is randomised from trial to trial. **k**, Group accuracy for the  
398 experiment in **j** (black trace: standard training, band: SEM, grey trace: full scramble  
399 control; n=33 training mice, n=5 control mice, n=9.3×10<sup>5</sup> trials). Throughout, isoamyl  
400 acetate and ethyl butyrate were used as odour stimuli.

401 **Fig. 3 | Odour correlation structure is encoded by olfactory bulb output neurons.**  
402 **a**, Schematic of the two-photon imaging approach (see also [Extended Data Fig. 7e](#)). **b**,  
403 Coronal olfactory bulb section showing GCaMP6f (green) expressed in projection  
404 neurons. Scale bar: 20μm. **c**, GCaMP6f fluorescence from mitral and tufted cells  
405 (maximum projection of 8000 frames). Responses from ROI \* in magnified inset 1 \* is  
406 shown in **d**. Scale bar: 20μm. **d**, Example traces of ROIs that show differential response  
407 kinetics to correlated (black) and anti-correlated (red) stimulation (mean of 24  
408 trials±SEM, f=20Hz, unpaired two-sided t-tests on 5s response-integrals) in  
409 anaesthetised and **e**, awake animals (mean of 16 trials±SEM, f=20Hz, unpaired two-sided  
410 t-tests). Odour presentation indicated in light blue. **f**, Calcium transients as colour maps  
411 for correlated (left) anti-correlated (middle) averaged trials and the difference between  
412 both odour stimulations (right) for the 5% of ROIs with the largest differential responses.  
413 **g**, Accuracy of linear classifier trained on several response windows (colour-coded, black:  
414 shuffle control) to correlated vs. anti-correlated stimuli at 20Hz (n=up to 680 ROIs from  
415 6 individual animals; mean±SD of 500 repetitions). **h**, Schematic of the extracellular  
416 recording approach. **i**, Example single unit of an odour response for correlated (black)  
417 and anti-correlated (red) stimuli shown as raster plot (top) and PSTH (mean±SEM) of  
418 spike times binned every 50ms (bottom); inset: average spike waveform (black) and  
419 1000 individual spike events (grey), scale bar: 100μV and 1ms. Odour presentation  
420 indicated in light blue. Two-sided Mann-Whitney U test comparing spike time  
421 distributions of correlated and anti-correlated trials during 4s after odour onset. **j**, Binned  
422 spike discharge over time shown as colour maps for all units, correlated (left), anti-  
423 correlated (middle) and the difference between both odour stimulations (right). **k**,  
424 Accuracy of linear classifier trained on the average 2s response to correlated vs. anti-  
425 correlated stimuli at 20Hz (yellow); green: 500ms window; blue 100ms window (n=up  
426 to 97 units from 6 individual animals; mean±SD of 1000 classifier repetitions; see  
427 Methods and [Extended Data Fig. 8](#)).

428 **Fig. 4 | Source separation using correlations of odour concentration fluctuations.**  
429 **a**, Simultaneous measurement of two odours (Odour 1: α-Terpinene; AT, Odour 2: ethyl  
430 butyrate; EB) using a dual-energy photoionisation detector ([Extended Data Fig. 10a-e](#),

431 **Supplementary Methods Fig. 2)** at  $d=40\text{cm}$ , presented either from one source or  
432 separated from each other by  $s=50\text{ cm}$ , with complex airflow in the laboratory. **b**,  
433 Correlation coefficients over all recordings for odours from the same source and for  
434 odour sources separated by  $s=10\text{-}50\text{cm}$  (EB vs. AT;  $n=61$  for Mix,  $n=71$  for each individual  
435 distance; unpaired two-sided t-test). Boxes indicate 25<sup>th</sup>–75<sup>th</sup> percentiles, thick line is  
436 median, whiskers are most extreme data points not considered outliers, see Methods. **c**,  
437 Example plumes used for training animals on a virtual source separation task to  
438 discriminate between odour stimuli derived from the same one source (Unrewarded, S-)  
439 and from separated sources recordings (Rewarded, S+). **d**, Example learning curve for a  
440 mouse trained to perform the virtual source separation task. Isoamyl acetate and ethyl  
441 butyrate were used as odour stimuli. **e**, Average accuracy over different variants of the  
442 task, calculated over the last 2400 trials of virtual source separation training ( $n=11$  mice,  
443  $p<0.0001$ , unpaired t-test, compared to chance performance), and subsequent stages  
444 where probe trials containing novel plume types are interleaved with the training set.  
445 Responses are compared between probe and training plumes within each stage. Probe  
446 plumes: odours fluctuate in a perfectly correlated manner, with a novel temporal  
447 structure (120 probe trials, in a segment of 2400 trials,  $n=11$  mice, paired t-test). Probe  
448 2Hz, 20Hz, 40Hz: Correlated/anti-correlated square pulse trains (50 probe trials per  
449 frequency, in a segment of 1650 trials,  $n=9$  mice). Responses to 2Hz, 20Hz and 40Hz  
450 probe trials were shuffled 10000 times to calculate chance performance; data is  
451 mean $\pm$ SD; unpaired two-sided t-test.

452 **Methods**

453 **Ethical compliance**

454 All animal procedures performed in this study were approved by the UK government  
455 (Home Office) and by the Crick Institutional Animal Welfare Ethical Review Panel.

456 **Mice**

457 All mice used for behavioural experiments were C57/Bl6 males ([Fig. 2 and 4, Extended](#)  
458 [Data Fig. 3-5 and 10](#)). In vivo imaging experiments were performed in 12-20 week old  
459 heterozygous OMP-cre (<sup>39</sup>; JAX stock #006668; [Fig. 1, Extended Data Fig. 2 and 6](#)) or  
460 Tbet-cre (<sup>40</sup>; Jax stock #024507; [Fig. 3, Extended Data Fig. 7](#)) mice crossed with the  
461 Ai95(RCL-GCaMP6f)-D line (<sup>41</sup>; JAX stock #028865) of either sex. Extracellular unit ([Fig.](#)  
462 [3 and Extended Data Fig. 8](#)) and whole-cell patch-clamp recordings ([Extended Data](#)  
463 [Fig. 9](#)) were performed in 5-8 week old C57/Bl6 males. Mice were housed up to 5 per  
464 cage in a 12/12h light/dark cycle. Food and water were provided ad libitum.

465 **Reagents**

466 All odours were obtained in their pure form from Sigma-Aldrich, St. Louis MO, USA. Unless  
467 otherwise specified, odours were diluted 1/5 with mineral oil in 15 ml glass vials (27160-  
468 U, Sigma-Aldrich, St. Louis MO, USA).

469 **Statistical analysis and data display**

470 To test for statistical significance between groups where appropriate we used either  
471 paired or non-paired student t-test or, for non-parametric data, the Mann-Whitney U test,  
472 or the Kolmogorov-Smirnov test to test the equality of probability distributions.  
473 Statistical test details and p-values are provided in figures and / or their respective figure  
474 legends. Unless specified otherwise, boxplots were plotted using the MATLAB boxplot  
475 function with the median depicted as a thick line and default maximal whisker length of  
476 1.5 \* (q3-q1) where q3 and q1 indicate the 75th and 25th percentile, respectively. If  
477 points were located outside this whisker range they were displayed individually as  
478 outliers. Violin plots show the median as a black dot and the first and third quartile by the  
479 bounds of black bars. Mouse cartoons were adapted from  
480 <https://scidraw.io/drawing/123 and /49>.

481 **High-speed odour delivery device**

482 The odour delivery device was based on a modular design of four separate odour  
483 channels, and consisted of an odour manifold for odour storage, a valve manifold for  
484 control of odour release and hardware for controlling and directing airflow through the  
485 system ([Fig. 1b](#)). The odour manifold was a 12.2x3.2x1.5 cm<sup>3</sup> stainless steel block with 4  
486 milled circular indentations (1 cm radius). Within each of these indentations was a  
487 threaded through-hole for installation of an input flow controller (AS1211F-M5-04, SMC,  
488 Tokyo, Japan) and an output filter (INMX0350000A, The Lee Company, Westbrook CT,  
489 USA). For each inset, the cap of a 15 ml glass vial (27160-U, Sigma-Aldrich, St. Louis MO,  
490 USA) with the centre removed was pushed in and sealed with epoxy resin (Araldite Rapid,

491 Huntsman Advanced Materials, Basel, Switzerland). This meant that glass vials could be  
492 screwed in and out of the insets for rapid replacement.

493 Solenoid valves typically limit high-fidelity odour stimulation resulting in odour rise  
494 times of several 10s of milliseconds under optimal conditions<sup>42</sup>. We thus employed high-  
495 speed micro-dispense valves with custom electronics for pulse-width modulation to  
496 maximize bandwidth: 4 VHS valves (INKX0514750A, The Lee Company, Westbrook CT,  
497 USA) were installed in a 4-position manifold (INMA0601340B, The Lee Company,  
498 Westbrook CT, USA) with standard mounting ports (IKTX0322170A, The Lee Company,  
499 Westbrook CT, USA). Each valve was connected to a corresponding odour position in the  
500 odour manifold with 10 cm Teflon tubing (TUTC3216905L, The Lee Company, Westbrook  
501 CT, USA). Each valve was controlled by digital commands via a spike-and-hold driver.  
502 Each digital pulse delivered to the spike-and-hold driver delivered a 0.5 ms, 24 V pulse to  
503 the valve (to open it), followed by a 3.3 V holding pulse lasting the rest of the duration of  
504 the digital pulse. This spike-and-hold input allowed for fast cycling of the valve without  
505 switching between 0 and 24 V at high frequencies to prevent from overheating the valve.  
506 Each valve was controlled by an individual spike-and-hold driver. Up to 4 drivers could  
507 be controlled and powered with a custom-made PSU consisting of a 24 V power input and  
508 a linear regulator to split the voltages into a 24 V and 3.3 V line, as well as control inputs  
509 taking digital signal input and routing it to the appropriate valve. Pulse profiles for  
510 calibration and stimulus production were generated with custom Python software  
511 (PyPulse, PulseBoy; [github.com/RoboDoig](https://github.com/RoboDoig)) allowing to define pulse parameters across  
512 multiple valves using a GUI.

513 To generate airflow through the olfactometer, a pressurised air source was connected to  
514 a filter (AME250C-F02, SMC, Tokyo, Japan) and demister (AMF250CF02, SMC, Tokyo,  
515 Japan) and then split into two separate lines, the input line and carrier line. Both lines  
516 were then connected to a pressure regulator (AR20-F01BG-8, SMC, Tokyo, Japan) and  
517 flow controller (FR2A13BVBN, Brooks Instrument, Hatfield PA, USA). The main line was  
518 then connected to the input of the valve manifold. The input line was split into 4 separate  
519 lines and connected to the input flow controllers (set to 0.25 L/min) on each odour  
520 position of the odour manifold. The output of the valve manifold was fitted with MINSTAC  
521 tubing (TUTC3216905L, The Lee Company, Westbrook CT, USA). Where the design was  
522 scaled up (e.g. to include 8 odour positions) the valve manifold outputs were connected  
523 and consolidated to a single output with 3-way connectors (QSMY-6-4, Festo, Esslingen  
524 am Neckar, Germany). Shape and reliability of odour pulses depended strongly on low  
525 volume headspace and low pressure levels (0.05 MPa). Flow change due to odour pulses  
526 was always compensated by mineral oil presentation (e.g. light grey in **Fig. 1ci**).  
527

### 528 *Odour characterisation*

529 Signal fidelities were calculated by first subtracting the average amplitude of troughs  
530 from the average amplitude of peaks during a pulse train and then subsequently dividing  
531 this peak-to-trough value by the difference of average peak amplitude subtracted by  
532 baseline amplitude ( $SignalFidelity = (meanPeak - meanTrough) / (meanPeak - baseline)$ ).  
533 This results in a value between 0 and 1, with 1 being perfectly modulated odour pulses.

534 **Behaviour**

535 *Automatic operant conditioning of cohorts of mice (AutonoMouse)*

536 In AutonoMouse, groups of mice (up to 25) implanted with an RFID chip are housed in a  
537 common home cage (**Fig. 2a**, for detailed description see<sup>24</sup>). Within the common home  
538 cage of AutonoMouse, mice have free access to food, social interaction and environmental  
539 enrichment. Water is not freely available in the system, but can be gained at any time by  
540 completion of an operant conditioning go/no-go task. To access these behavioural tasks,  
541 mice must leave the home cage and enter a behavioural area. This behavioural area  
542 contains the odour port and a lick port through which water rewards can be released. The  
543 lick port is also connected to a lick sensor, which registers the animal's response (its lick  
544 rate) in response to the task stimuli. As animals can only gain their daily water intake by  
545 completing behavioural tasks, mice are motivated to complete long sequences of trials  
546 without manual water restriction.

547

548 *Training on temporally structured odours*

549 We aimed to probe whether mice could perceive a particular temporal feature of  
550 naturally occurring odour signals: temporal correlations between odour signals. In  
551 particular, we aimed to investigate this question with the simplest possible case: whether  
552 mice could discriminate perfectly correlated from perfectly anti-correlated odour stimuli.  
553 All tasks followed a standard go/no-go training paradigm. Animals were presented with  
554 two odours presented in either a correlated pattern or an anti-correlated pattern (**Fig. 2d**  
555 and **Extended Data Fig. 4a-c**). For roughly half of all animals, the correlated pattern was  
556 S+ (rewarded) and the anti-correlated pattern was S- (unrewarded); in the other half of  
557 the group this reward valence was reversed. All stimuli were 2 s long. A water reward  
558 could be gained by licking such that licking was detected for at least 10% of the stimulus  
559 time during an S+ presentation (a "Hit"). Licking for the same amount of time during S-  
560 presentation resulted in a timeout interval of 7 seconds. In all other response cases, the  
561 inter-trial interval was 3 seconds and no water reward was delivered.

562

563 *Stimulus structure*

564 All anti-correlated and correlated stimuli on each trial followed a common pattern in  
565 their construction. Generally, wherever an odour position is inactivated a blank position  
566 should be activated to compensate for flow change. There should also be no consistent  
567 differences in the amount of odour or flow released during the stimulus between  
568 correlated and anti-correlated stimuli. The detailed algorithm for stimulus generation is  
569 as follows:

570

571 I. Correlated or anti-correlated/uncorrelated odour pulses (**Fig. 2d-k and Extended**  
572 **Data Fig. 3 and 5**)

- 573 1. The stimulus is chosen to be correlated or anti-correlated/uncorrelated.
- 574 2. A set of 1-2 positions each for odour 1 and odour 2 and 2-3 positions for blank are  
575 randomly chosen from a pre-defined subset of 6 of the 8 total positions. For

example, a valid combination could be odour 1 at position 1, 2; odour 2 at position 5; and blank at position 3 and 7. (see [Fig. 2g and Extended Data Fig. 4b](#))

3. A guide pulse is created at the desired frequency (e.g. 2 Hz pulse with 50% duty, see [Supplementary Methods Fig. 1c](#)) for all positions that follows the chosen stimulus structure.
4. The relative contributions of each position to the total stimulus are randomly generated. At each time point in the stimulus, only two position types should be active (e.g. odour 1 and blank for an anti-correlated stimulus) so the maximum contribution for any position type is 50% of the total release amount. Where two positions have been chosen for a position type, their relative contributions should add to 50% ([Extended Data Fig. 4b](#)).
5. The guide pulses are pulse-width modulated according to the relative contributions of each position ([Supplementary Methods Fig. 1c](#)). Pulse-width modulation (PWM) is at 500 Hz with some added jitter in the duty to avoid strong tone generation.
6. For uncorrelated pulses, temporal offsets are added in one channel according to a distribution of time delays that follow the desired correlation structure between the two odour pulses ([Extended Data Fig. 3e,f](#)).

II. “One source” and “Source separated” naturalistic plumes ([Fig. 4c-e and Extended Data Fig. 10](#))

1. The stimulus is chosen to be “One source” or “Source separated”.
2. A plume bank of plume pairs obtained from indoor PID recordings is created. Each trial will contain 2 plumes, each representing one odour recording originating from one source or from sources positioned 50 cm apart. To maintain consistency in trial length between behaviour experiments, a 2 s time window from each plume was selected from the middle of each 5 s recording, such that odour was always present in the first 500ms of the trial. Trials where the correlation of the 2 s window was vastly different from the original 5 s were excluded from the plume bank. This procedure resulted in a plume bank containing 72 plume pairs for the separated source condition and 48 plume pairs for the one source condition.
3. An odour plume pair is randomly selected from the plume bank, from the corresponding category.
4. The odour that will be used to replicate each plume in a pair and the positions in the odour delivery device that will be used for that purpose are randomly assigned, as described previously. For each odour valve active, a blank valve will also be activated to produce an “anti-plume” structure, to compensate for the changes in flow created by odour delivery.
5. Plumes are recreated from the chosen PID recordings. Each trace is normalised to between 0 and 1, and then converted into a series of binary opening and closing times. The length of the openings and closings relate directly to the value of the normalised signal, a value of one translates to a continuous opening, and a value of

618 zero translates to continuously closed. This series of openings and closings are  
619 relayed to the valves and the resulting output resembles the original plume.  
620

621 III. Perfectly correlated plume trials (probe trials, [Fig. 4e](#))

622 1. A 2 s window is chosen from the source separated plume bank (plume structures  
623 previously associated with opposite reward valence – 5 trials) or from independent  
624 plume recordings obtained in a different environment than the original recordings  
625 (completely novel plume structures – 10 trials).  
626 2. The chosen plume structure is replicated using both odour channels, resulting in a  
627 plume where both odour components fluctuate in a perfectly correlated manner.  
628

629 IV. Frequency discrimination pulses ([Fig. 2c and Extended Data Fig. 3a-d](#))

630 1. Two frequencies are chosen for discrimination (e.g. 2 Hz vs. 20 Hz).  
631 2. For each trial one of the frequencies is chosen for presentation.  
632 3. Valves are selected for presentation of both odours.  
633 4. A guide pulse is created for each odour channel that pulses at the desired trial  
634 frequency with 50% duty, such that pulse alternates between channels at the given  
635 frequency.  
636 5. Guide pulses are pulse-width-modulated as for correlated/anti-correlated stimuli.  
637

638 *Task structure for the correlation experiment ([Fig. 2d-k, Extended Data Fig. 3-5](#))*

639 Task frequency was randomised from trial to trial in a range between 2-81 Hz. The choice  
640 of frequency was with weighted probability divided into 3 frequency bands. E.g. this task  
641 could be arranged such that 2-20 Hz would be chosen with  $P = 0.6$ , 21-40 Hz with  $P = 0.3$   
642 and 41-81 Hz with  $P = 0.1$ . Within each of these frequency bands, the choice of individual  
643 task frequency was based on a uniform distribution. Thus, few trials were performed for  
644 frequencies exceeding 40 Hz resulting in more “noisy” behavioural performance data in  
645 [Fig. 2k](#).  
646

647 *Onset detection*

648 For the onset detection experiments ([Extended Data Fig. 5f-i](#)) animals were trained to  
649 discriminate perfectly correlated (e.g. S+) from perfectly anti-correlated stimuli (e.g. S-)  
650 and probed with partially altered stimuli where the onset (first cycle) of the probe S+  
651 stimuli was anti-correlated and probe S- stimuli where the onset (first cycle) was  
652 correlated. Performance during these probe trials is then compared to the average  
653 performance during training ( $perf_{train}$ ).

654 We calculated the expected average animal performance on the probe trials based on two  
655 models (prediction data, [Extended Data Fig. 5f,g](#)): Model 1 assumed the animals were  
656 taking any part of the stimulus into account equally when making a decision. Model 2  
657 assumed that only the onset of the stimulus would contribute to discrimination. Thus for  
658 Model 1, a stimulus of frequency  $f$  (e.g. 10 Hz) that was sampled for  $t_{sample}$  consisted of a  
659 “shifted” onset component of one cycle for S+ ( $1/f$ ) and half a cycle for S- ( $0.5/f$ )

660 corresponding to a fraction of  $frac_{onset} = 1/f/t_{sample}$  of the entire stimulus and a  
661 “normal” residual ( $frac_{res} = 1 - frac_{onset}$ ). Thus, the predicted probe trial performance  
662 would be:

663 (1)  $predicted\ probe\ trial\ perf_{entire} = perf_{train} \times frac_{res} + (1 - perf_{train}) \times frac_{onset}$

664 In **Extended Data Fig. 5i** this prediction was calculated for the following parameters:  
665 Sniff frequency: 6 Hz, inhalation fraction: 0.2, stimulus sampling time: 0.7 s, In **Extended**  
666 **Data Fig. 5g** sampling time was varied as indicated.  
667

668 For Model 2, ignoring inhalation timing, the prediction would be that preference would  
669 be reversed (as onset correlations during probe trials are reversed). However, this  
670 ignores the fact that odour stimuli during the exhalation period might not be detected.  
671 Thus, to more accurately predict animals’ performance for Model 2, we assume that the  
672 part of the stimulus that is detected as the “onset” is the first odour pulse during an  
673 inhalation phase. During the probe trial, this will be the “inverted” first cycle if the  
674 stimulus begins either during the inhalation phase or at most  $1/f$  before the inhalation  
675 (then inhalation would start during the inverted first cycle of the probe trial). The  
676 probability of this occurring is  $perf_{onset} = (dur_{inh} + 1/f) / dur_{sniff}$  with  $dur_{inh}$  and  
677  $dur_{sniff}$  being inhalation and sniff duration respectively (provided  $dur_{inh} + 1/f <$   
678  $dur_{sniff}$ ). Predicted probe trial performance for an “onset only” model would thus be:

679 (2)  $predicted\ probe\ trial\ perf_{onset} = perf_{train} \times (1 - perf_{onset}) + (1 - perf_{train}) \times perf_{onset}$

680 **Extended Data Fig. 5f,g** displays the predictions of these two models in comparison to  
681 the experimental data for a broad range of respiration patterns. The “prediction data” in  
682 **Extended Data Fig. 5i** shows model predictions assuming typical sniff and sampling  
683 parameters as indicated above (Sniff frequency: 6 Hz, inhalation fraction: 0.2, stimulus  
684 sampling time: 0.7 s).  
685

#### 686 *Controls*

687 Control valves could be automatically added to the random frequency task. These tasks  
688 produced their stimuli based on a subset of 6 valves and control valves could be added  
689 automatically after a set period of trials to force the algorithm to produce stimuli from all  
690 8 valves (see **Fig. 2g,i** switch control and **Extended Data Fig. 4i-k**).  
691

692 A subgroup of animals was created in which the valve map was scrambled, as an ongoing  
693 control against animals learning extraneous variables in the task (see **Fig. 2k**, scramble  
694 control). The valve map was scrambled in the following way: One blank to odour 1, one  
695 odour 2 to blank, one odour 1 to odour 2 and one odour 1 to blank. Every few days all  
696 odour bottles were cleaned and replaced, odour positions changed and valves re-  
697 assigned<sup>43</sup>.

#### 698 *Airflow and sound recordings*

699 Airflow and sound were recorded in AutonoMouse during trials at different frequencies  
700 to ensure that the temporal structure of the odour is the only parameter that varies over  
trials and that no tactile or auditory cues were present in the stimulus. A flow sensor

701 (AWM5101VN, Honeywell, USA) and a microphone (NTG1, RØDE, Australia) were placed  
702 in close proximity to the AutonoMouse odour port. In total, 286 trials were recorded (2  
703 Hz: n = 75 correlated, n = 70 anti-correlated; 40 Hz: n = 69 correlated, n = 72 anti-  
704 correlated) using Audacity for sound and Spike2 (Cambridge Electronic Design, UK) for  
705 flow signals. Airflow and sound signal underwent spectral analysis (Fourier transform),  
706 as well as linear classification analysis ([Extended Data Fig. 4d-g](#)).

707

#### 708 *Training on naturalistic plumes*

709 One group of animals (n = 12) were trained to discriminate between plumes derived from  
710 those originating from one source (S-, unrewarded) or from separated sources (S+,  
711 rewarded), using 2 s long stimuli produced as described above from the recordings  
712 shown in [Fig. 4a](#). An additional 12 animals trained simultaneously on the reverse reward  
713 valence did not pass the performance criterion within the given timeframe and were not  
714 carried forward to probe trials.

715 To test whether correlation structure was a feature used by mice to perform the virtual  
716 source separation task, probe trials were introduced randomly at a frequency of  
717 approximately 1 in 11 trials, with every instance of a probe trial repeated every 330 trials.  
718 Probe trials consisted of perfectly correlated plumes or correlated/uncorrelated square  
719 pulses produced as described above, presented at 3 different frequencies: 2 Hz, 20 Hz, 40  
720 Hz. The feedback for probe trials was the same as for a training trial, with a reward or  
721 time-out given based on the response of the mouse. No change in performance across  
722 repeated presentation of the probe trials was observed indicating that performance was  
723 not due to putative rapid re-learning. Of the 12 mice exposed to this protocol, a total of 9  
724 mice reached all phases of the experiment.

725

#### 726 *Cohorts*

727 The correlation discrimination experiment was performed in 3 separate experimental  
728 cohorts ([Fig. 2, Extended Data Fig. 3 -5](#): group 1, n = 14; group 2, n = 25 (one animal did  
729 not successfully pass the pre-training); [Fig. 4, Extended Data Fig. 10](#): group 3, n = 24,  
730 see above). Each cohort was organised into several subgroups, which performed slight  
731 variations of the behavioural tasks in terms of reward valence and valves utilised, but  
732 with the same underlying task aim. Half of the animals in each subgroup were trained on  
733 correlated stimuli as the S+ rewarded condition, with the other half trained on anti-  
734 correlated as rewarded. Animals were further subdivided into groups, which were  
735 trained on different subsets of valves as standard in the 8-channel olfactometer. For each  
736 cohort, mice were once assigned to each of these subgroups based on performance in a  
737 simple pure odour discrimination at the beginning of the experiment - group  
738 membership was randomised until no significant (ANOVA, Tukey-Kramer) differences in  
739 performance could be extracted between these subgroups on this task.

740

741 *Data analysis*  
742 AutonoMouse behavioural data was converted to MATLAB data format using the  
743 Conversion module of the Python autonomouse-control package  
744 ([github.com/RoboDoig](https://github.com/RoboDoig)). All subsequent analysis was performed with custom-written  
745 MATLAB scripts unless otherwise specified.  
746 All behavioural performance within a specified trial bin was calculated as a weighted  
747 average of S+ vs. S- performance:

$$748 \quad \text{performance} = \frac{(\text{Hit} / S+) + (\text{CR} / S-)}{2}$$

749 Where S+ is the total number of rewarded trials, S- is the total number of unrewarded  
750 trials, Hit is the total number of rewarded trials in which a lick response was detected, CR  
751 (correct rejection) is the total number of unrewarded trials in which no lick response was  
752 detected.

753 For random stimulus pulse frequency experiments (e.g. **Fig. 2j,k**) trials were binned  
754 approximately by half-octave for performance analysis. The exact intervals were  $f(\text{Hz}) =$   
755  $[2, 3, 4, 5, 6:7, 8:10, 11:13, 14:17, 18:22, 23:29, 30:37, 38:48, 49:62, 63:81]$ . Reaction time  
756 ([Extended Data Fig. 5](#)) was calculated from S+ trials for each animal as the time to the  
757 first lick after stimulus onset. For presentation of learning curves (**Fig. 2h, 4d**) accuracy  
758 was calculated over 100-trial sliding windows.

759 Motion magnification of the respiration camera video recordings ([Extended Data Fig. 5](#)  
760 **and Supplementary Video 2**) was performed with phase-based video motion  
761 processing with correction for large body movements based on MATLAB scripts by <sup>44</sup>  
762 (phaseAmplifyLargeMotions). Parameters for phase amplification were: blurring  $\sigma = 1$ ,  
763 magnification  $\alpha = 50$ , amplification in frequency band between 2-13 Hz. Following  
764 magnification, static ROIs for each video were selected in Bonsai ([http://www.kampff-  
765 lab.org/bonsai/](http://www.kampff-lab.org/bonsai/), <sup>45</sup>) over the animal flank. An adaptive binary threshold was applied to  
766 the ROI to segment the animal body from the video background. Respiration rate was  
767 extracted from the total size of the ROI occupied by the body over time.

## 768 **Olfactory sensory neuron population model**

### 769 *Overview*

770 We modelled the olfactory sensor neuron (OSN) population as noisy integrate-and-fire  
771 neurons integrating a filtered odour pulse and with independent (cell-specific) noise to  
772 qualitatively match experimental data<sup>46</sup>. The square of the resulting mean population  
773 firing rate was convolved with a calcium imaging filter to produce a model of the observed  
774 calcium imaging signal. All code and related data for the model can be found at  
775 <https://github.com/stootoon/crick-osn-model-release>.  
776

### 777 *Odour Input Current*

778 The olfactory input current  $I_t$  to each OSN was modelled as a filtered version of the odour  
779 pulse input  $O_t$ :

$$780 \quad \tau_C \frac{dI_t}{dt} = -I_t + O_t$$

781 This filtering models filtering of the nasal cavity, transport through the mucous, and  
782 chemical transduction from odour concentration to receptor channel opening.

783

#### 784 *Olfactory Sensory Neurons*

785 Each OSN was modelled as a noisy integrate-and-fire neuron. Each OSN membrane  
786 performs a noisy integration of the olfactory input current  $I_t$  so that the membrane  
787 voltage  $V_t$  satisfies the following stochastic differential equation:

$$788 \quad \tau_V dV_t = (I_t - V_t)dt + \sigma dB_t.$$

789 Here  $B_t$  is standard Brownian motion and  $\sigma$  is the standard deviation of the membrane  
790 voltage noise. The OSN generates a spike whenever its membrane voltage exceeds a  
791 spiking threshold  $\theta$ :

$$792 \quad S_t = \begin{cases} 1 & \text{If } V_t \geq \theta; \\ 0 & \text{otherwise.} \end{cases}$$

793

794 Upon spiking the membrane voltage is clamped to a refractory voltage  $V_{ref}$  for a period  
795 of  $t_{ref}$  seconds. The mean instantaneous firing rate of the population is computed as

$$796 \quad \bar{S}_t = \frac{1}{N} \sum_{n=1}^N S_t^n$$

797 where  $S_t^n$  is the spiking activity of OSN  $n$ .

798

#### 799 *Calcium imaging signal*

800 To model the calcium imaging signal the mean firing rate is squared and convolved with  
801 the imaging kernel  $h_t$  to form the calcium imaging signal  $C_t$ :

$$802 \quad C_t = (\bar{S}_t^2) * h_t.$$

803 The calcium imaging kernel is an alpha function:

$$804 \quad h_t = t e^{-t/\tau_h}$$

805 A list of parameters is given in [Supplementary Table 1](#). All parameters were fit  
806 manually: Parameters  $\tau_C$ ,  $\tau_V$  and  $\sigma$  were set to produce a qualitative match in time courses  
807 between model membrane voltage traces and the suction current traces in Figure 2 of  
808 reference <sup>46</sup>. The remaining parameters were adjusted to produce a qualitative fit  
809 between model and the dynamics of the observed calcium imaging traces.

810

## 811 **Generating model glomeruli**

### 812 *Overview*

813 We generated 100 model glomeruli by randomly varying a subset of the model OSN  
814 parameters described in the previous section ( $\tau_V$ ,  $\tau_C$ ,  $\sigma$ ,  $\theta$ ,  $a$ ). Specifically, we picked the  
815 parameters of each glomerulus by selecting uniformly within  $\pm 25\%$  of the centre value  
816 of each parameter. All 5000 OSNs within each glomerulus had the same parameters, and  
817 differed only due to the random noise applied to their membrane voltages. The range of  
818 variation is shown in [Supplementary Table 2](#).

819

820  
821 The effect of concentration was modelled by linear scaling of the input waveforms. For  
822 each setting of PPI and concentration the model was run to simulate 25 consecutive trials  
823 of length 2.5 seconds each, with the odour onset at 0.1 seconds into each trial. The first 5  
824 trials of data were discarded to allow the model to 'settle,' yielding 20 trials for each  
825 condition that were used in subsequent analyses ([Extended Data Fig. 1g,h, Extended](#)  
826 [Data Fig. 2j,k](#)).

827

## 828 **Classifying glomerular outputs**

829 *Predictors*

830 The predictors used for classification were the response integrals for each glomerulus,  
831 defined as the instantaneous mean firing rate of the OSNs in the glomerulus, filtered by  
832 the Ca<sup>2+</sup> imaging filter (see section "Olfactory sensory neuron population model") and  
833 summed over the 2 seconds following odour onset in each trial. Since the scale of the  
834 responses is arbitrary, we scaled the response integrals by their overall standard  
835 deviation, computed over glomeruli and trials.

836

837 *Labels*

838 Trials were labelled by their paired-pulse interval (PPI), or a combination of PPI and  
839 concentration, depending on the task.

840

841 *Classifiers*

842 The classifiers used were support vector machines with linear kernels and l2  
843 regularization as implemented by the 'LinearSVC' function of the Python scikit-learn  
844 library. The setting of the penalty parameter C and whether or not to learn an intercept  
845 were determined by cross-validation with scikit-learn's 'GridSearchCV'. The values of C  
846 considered ranged in powers of 10 from 10<sup>-4</sup> to 10<sup>4</sup>.

847 *Computing Decoding Accuracy*

848 The decoding accuracy for a given subset of n glomeruli was computed as the average  
849 accuracy over 10 cross-validation trials for the results in [Extended Data Fig. 1h](#), and 40  
850 cross-validation trials for the results in [Extended Data Fig. 2j,k](#). In each cross-validation  
851 trial, the classifier was trained on a random 90% of the trials, tested on the remaining  
852 10%, and the accuracy recorded. The random subsets were stratified i.e. constrained to  
853 have the same fraction of trials from each class as the full dataset when possible. The  
854 mean accuracy across cross-validation trials was recorded as the accuracy for that subset.  
855 To compute the shuffled performance, the labels of the training and test trials were  
856 shuffled in each cross-validation trial before the classifier accuracy was computed.

857

858 *Decoding PPI from the responses of model glomeruli*

859 To determine how decoding accuracy was affected by the size of the population used we  
860 selected a random subset of n glomeruli and computed the decoding accuracy as  
861 described above. This was repeated for 256 random subsets of n glomeruli generating

862 256 unshuffled and 256 shuffled accuracies. The subset size  $n$  was varied from 1 (using  
863 only a single glomerulus) to 100 (using the full population; [Extended Data Fig. 1h](#)). Note  
864 that for  $n \geq 99$ , some subsets are likely to have been repeated because there are fewer  
865 than 256 possible subsets of size 99 and 100. The observed variability in accuracy in  
866 those cases is then due mainly to the random determination of training and testing trials.  
867

868 *Decoding PPI and concentration from the responses of model glomeruli*

869 To compute the decoding accuracy when decoding PPI and concentration, we followed a  
870 very similar procedure to the previous section, but fixed the population size at the  
871 maximum of 100 and varied the stimulus concentration from 0.5 to 5 in steps of 0.5 to  
872 cover a factor of 10 range in concentration as used in the experimental data ([Extended](#)  
873 [Data Fig. 2j-m](#)). For comparison, the results in [Extended Data Fig. 1h](#) were for a  
874 concentration of 1. Decoders were trained to extract just concentration, or PPI and  
875 concentration.

876 **In vivo two-photon imaging**

877 *Surgical and experimental procedures*

878 Prior to surgery all utilised surfaces and apparatus were sterilised with 1% trigene. Mice  
879 were anaesthetised using a mixture of fentanyl/midazolam/medetomidine (0.05 mg/kg,  
880 5 mg/kg, 0.5 mg/kg respectively). Depth of anaesthesia was monitored throughout the  
881 procedure by testing the toe-pinch reflex. The fur over the skull and at the base of the  
882 neck was shaved away and the skin cleaned with 1% chlorhexidine scrub. Mice were then  
883 placed on a thermoregulator (DC Temperature Controller, FHC, ME USA) heat pad  
884 controlled by a temperature probe inserted rectally. While on the heat pad, the head of  
885 the animal was held in place with a set of ear bars. The scalp was incised and pulled away  
886 from the skull with four arterial clamps at each corner of the incision. A custom head-  
887 fixation implant was attached to the base of the skull with medical super glue (Vetbond,  
888 3M, Maplewood MN, USA) such that its most anterior point rested approximately 0.5 mm  
889 posterior to the bregma line. Dental cement (Paladur, Heraeus Kulzer GmbH, Hanau,  
890 Germany; Simplex Rapid Liquid, Associated Dental Products Ltd., Swindon, UK) was then  
891 applied around the edges of the implant to ensure firm adhesion to the skull. A  
892 craniotomy over the left olfactory bulb (approximately 2 x 2 mm) was made with a dental  
893 drill (Success 40, Osada, Tokyo, Japan) and then immersed in ACSF (NaCl (125 mM), KCl  
894 (5 mM), HEPES (10 mM), pH adjusted to 7.4 with NaOH, MgSO<sub>4</sub>·7H<sub>2</sub>O (2 mM),  
895 CaCl<sub>2</sub>·2H<sub>2</sub>O (2 mM), glucose (10 mM)) before removing the skull with forceps. The dura  
896 was then peeled back using fine forceps. A layer of 2% low-melt agarose diluted in ACSF  
897 was applied over the exposed brain surface before placing a glass window cut from a  
898 cover slip (borosilicate glass 1.0 thickness) using a diamond knife (Sigma-Aldrich) over  
899 the craniotomy. The edges of the window were then glued with medical super glue  
900 (Vetbond, 3M, Maplewood MN, USA) to the skull.

901 Following surgery, mice were placed in a custom head-fixation apparatus and transferred  
902 to a two-photon microscope rig along with the heat pad. The microscope (Scientifica  
903 Multiphoton VivoScope) was coupled with a MaiTai DeepSee laser (Spectra Physics, Santa

904 Clara, CA) tuned to 940 nm (<50 mW average power on the sample) for imaging. Images  
905 (512 x 512 pixels) were acquired in SciScan (Scientifica, UK) with a resonant scanner at  
906 a frame rate of 30 Hz using a 16x 0.8 NA water-immersion objective (Nikon). The output  
907 of a 4-channel version of the temporal olfactometer described above was adjusted to  
908 approximately 1 cm away from the ipsilateral nostril to the imaging window, and a flow  
909 sensor was placed next to the contralateral nostril for continuous respiration recording.  
910

#### 911 *Awake recordings*

912 For implantation of the head-plate, mice were anaesthetized with isoflurane in 95%  
913 oxygen (5% for induction, 1.5-3% for maintenance). Local (mepivacaine, 0.5% s.c.) and  
914 general analgesics (carprofen 5 mg/kg s.c.) were applied immediately at the onset of  
915 surgery. After surgery, animals were allowed to recover for 7 days with access to wet diet  
916 and, after recovery, habituated to the head-fixed situation for at least 15 min on three  
917 consecutive days preceding the imaging experiment.  
918

#### 919 *Odour stimulation*

920 For paired-pulse experiments, ethyl butyrate was diluted in mineral oil at the ratio of 1:5  
921 and installed into a 4-channel version of the high-speed odour delivery device (15 ml per  
922 vial) along with two blank positions (15 ml mineral oil). Odour concentration range was  
923 adjusted over 10 steps on a logarithmic scale with a factor of 1.25 by modulating odour  
924 pulse-width.

925 For correlated vs. anti-correlated stimulus experiments, stimuli were generated from  
926 mixtures of physically mixed monomolecular odorants in order to ensure high  
927 probability of finding odour responsive cells in the dorsal olfactory bulb using custom  
928 Python Software (PulseBoy). Binary mixtures were diluted in mineral oil at the ratio of  
929 1:5 and installed into a 4-channel version of the high-speed odour delivery device (15 ml  
930 per vial) along with two blank positions (15 ml mineral oil). Mix 1: ethyl butyrate + 2-  
931 hexanone, mix 2: isoamyl acetate + cineole. During glomerular imaging experiments  
932 ([Extended Data Fig. 6](#)), six odours (A-F) where presented either individually or in pairs:  
933 A (ethyl butyrate), B (2-hexanone), C (isoamyl acetate), D (cineol), E (ethyl tiglate) and F  
934 ((+)-fenchone). For all stimuli, odour valve offsets were compensated by opening a  
935 corresponding blank position valve to ensure no global flow changes occurred over the  
936 course of the stimulus. All stimuli were repeated between 16-50 times with at least 15 s  
937 inter-stimulus interval.  
938

#### 939 *Data analysis*

940 For M/TC imaging, motion correction, segmentation and trace extraction were  
941 performed using the Suite2p package (<https://github.com/MouseLand/suite2p><sup>47</sup>).  
942 Putative neuronal somata and dendritic segments were automatically identified by  
943 segmentation and curated manually. Soma and neuropil fluorescence traces were  
944 extracted and neuropil fluorescence was subtracted from the corresponding soma trace.  
945 Further analysis was performed with custom written scripts in MATLAB.

946 M/TCs were recorded in 17 fields of view (FOV) from 6 individual Tbet-cre:Rosa-  
947 GCaMP6f animals, with  $40 \pm 9.23$  (mean  $\pm$  SD; range 27-48) cells per FOV and  $30.25 \pm$   
948 12.97 (mean  $\pm$  SD; range 7-53) M/TC dendrites,

949 For glomerular imaging experiments, ROIs corresponding to glomeruli were manually  
950 delineated based on the mean fluorescence image. Fluorescence signal from all pixels  
951 within each ROI was averaged and extracted as time series.  $\Delta F/F = (F-F_0)/F_0$ , where  $F =$   
952 raw fluorescence and  $F_0$  was the median of the fluorescence signal distribution.

953 Glomerular signals from a total of 15 individual OMP-cre:Rosa-GCaMP6f animals were  
954 recorded with  $28 \pm 4.34$  (mean  $\pm$  SD; range 20-36) glomeruli per animal ([Extended Data  
955 Fig. 6a](#)).

956 Where the odour stimulus was not inhalation-triggered, traces were post hoc aligned to  
957 the first inhalation after odour onset. Calcium response integrals were calculated for a  
958 range of window durations starting from odour onset (100-5000 ms). To analyse how  
959 well odour responses predicted stimulus correlation on a trial-to-trial basis, we  
960 generated a linear discriminant classifier from the data set and analysed prediction  
961 accuracy. For the classifier, we performed 50% holdout validation, splitting the data  
962 randomly into a training set and test set with equal numbers of samples. We then  
963 performed linear discriminant analysis on the training data set to determine the best  
964 linear boundary between 10 vs. 25 ms pulse interval stimulations or correlated vs. anti-  
965 correlated data. Classifier performance was then validated on the test data set. To  
966 determine the effect of number of ROIs used on classifier performance, we iteratively  
967 trained multiple classifiers on random subsets of ROIs with increasing numbers of ROIs  
968 within each set. For each ROI subset size, 100 classifiers were trained and the mean  $\pm$  SD  
969 of their performance accuracy was calculated. All classifier analysis was performed on  
970 individual, unaveraged trials.

971

972 *Glomerular imaging classifiers in [Extended Data Fig. 6k,l](#)*

973 The classifiers used in [Extended Data Fig. 6k,l](#) were trained separately for each odour  
974 pair, each frequency, and each time window. The inputs for classification were the  
975 averaged responses of the 145 glomeruli in a given time window for 24 odour  
976 presentation trials, where the odours were fluctuating in a correlated manner in half of  
977 the trials, and in an anti-correlated manner in the remaining half. Within the correlated  
978 and anti-correlated subsets of trials, half had the first odour in the pair phase-shifted by  
979 180 degrees, and the remaining half had no phase shift. The classification task was to  
980 determine whether the glomerular responses in a given trial were evoked by correlated  
981 or anti-correlated odour fluctuations.

982

983 Because we had far fewer trials (24) than glomeruli (145) it was important to use  
984 regularized classifiers to avoid overfitting. To promote interpretability of the decision  
985 boundaries learned by the classifiers we opted for sparsity-promoting regularizers and  
986 settled on the Lasso, evaluated as a classifier by taking the sign of its output computed  
987 after the addition of a small amount of noise (to decide ambiguous classifications). The  
988 implementation of the Lasso we used was 'LassoLarsCV' provided by the Python scikit-

989 learn library because it converged readily, gave very good classification performance, and  
990 automatically tuned the weighting of the sparsity penalty. Inputs to the classifier were  
991 standardized to have mean zero and unit variance across trials. We found that it was  
992 important to learn the classification weights without intercept to avoid overfitting.  
993

994 The performance of a classifier was determined by cross-validation, where in each cross-  
995 validation iteration, the classifier was trained on a random ~90% of the trials (21 trials)  
996 and tested on the remaining ~10% (3 trials), and the test accuracy recorded. The random  
997 subsets were selected in a stratified manner, meaning that the fraction of correlated and  
998 anti-correlated trials in the subset were kept as close as possible to their fraction in the  
999 full dataset (50/50). This meant that 10 of the 21 training trials were of one type and 11  
1000 of the other. This procedure was performed for 10 cross-validation iterations, and the  
1001 average performance over these repeats was recorded as the performance of the  
1002 classifier. The shuffled performance was computed the same way but with training and  
1003 test labels shuffled in each iteration. The entire procedure was then repeated for each of  
1004 100 different random seeds to produce a distribution of classification accuracies, whose  
1005 means and standard deviations are plotted in [Extended Data Fig. 6k,l](#).  
1006

1007 Because we used a sparsity-promoting classifier it was straightforward to determine  
1008 which glomeruli were contributing to a particular classification decision. We found that  
1009 if we used all 145 glomeruli available then frequently glomeruli would be selected for  
1010 noisy fluctuations of their responses that were by chance ‘informative’ for the  
1011 classification. To avoid the inclusion of such noisy responses, we filtered glomeruli for  
1012 responsivity. To determine the responsivity of a glomerulus, the mean  $\bar{X}_{glom,baseline}$  and  
1013 standard deviation  $\sigma_{glom,baseline}$  of its responses pooled across all baseline bins (defined  
1014 as the 3 seconds before odour onset) and across all trials for the given odour pair and  
1015 frequency were first computed. A Z-score was then computed for its averaged response  
1016 for the given time bin and for each trial by comparing this response to the baseline  
1017 activity according to

$$1018 \quad Z_{glom,trial} = \frac{X_{glom,trial} - \bar{X}_{glom,baseline}}{\sigma_{glom,baseline} / \sqrt{n_{wnd}}},$$

1019 where  $X_{glom,trial}$  is the response of the glomerulus in the given time window and  $n_{wnd}$  is  
1020 the number of time bins constituting the window. The scaling of the baseline standard  
1021 deviation is to account for the reduction in variance due to the averaging over time bins  
1022 used to compute the response. A glomerulus was considered responsive in a given trial if  
1023 the absolute value of its Z-score as computed above was greater than 1 on three-quarters  
1024 or more of the trials. Such a thresholding ensured that the number of responsive  
1025 glomeruli was almost always zero before odour onset, but rose to a peak ~125 of the 145  
1026 glomeruli available when 2 s windows were used. Reducing the window size reduced the  
1027 peak number of glomeruli, but at least 25 glomeruli were used during the peak responsive  
1028 period in all cases, and frequently many more. This filtering also meant that some time

1029 windows late in the response contained no responsive glomeruli for some window sizes,  
1030 which explains the 'patchiness' observed in **Extended Data Fig. 6k,l.**

1031 **Extracellular recordings**

1032 *Surgical and experimental procedures*

1033 5-8 week old C57BL/6Jax mice were anaesthetised using a mixture of ketamine/xyazline  
1034 (100mg/kg and 10mg/kg respectively) by intraperitoneal (IP) injection. An IP line was  
1035 inserted after the initial injection to allow for easier and more regular subsequent  
1036 injections of anaesthetics. Surgery was carried out as described above for two-photon  
1037 imaging, up until the application of agar and cranial window.

1038 Following surgery, mice and custom platform were transferred to the extracellular  
1039 recording set up. A flow sensor (A3100, Honeywell, NC, USA) was placed in front of the  
1040 contralateral nostril whilst an output from the temporal olfactometer was positioned in  
1041 front of the ipsilateral nostril. A Ag/Ag<sup>+</sup>Cl<sup>-</sup> reference coil was immersed in the well, over  
1042 the left hemisphere of the skull. The reference wire was connected to both the reference  
1043 and ground of the amplifier board (RHD2132, intan, CA, USA), which was connected  
1044 (Omnetics, MN, USA) to a head-stage adapter (A32-OM32, NeuroNexus, MI, USA). A 32-  
1045 channel probe (A32-Poly3, NeuroNexus, MI, USA) was connected to the adapter, and the  
1046 tip of the probe was manoeuvred to be positioned 1-2cm above the craniotomy. The  
1047 adapter and probe were held above the craniotomy using a micromanipulator (PatchStar,  
1048 Scientifica, UK) set at 90 degrees to the surface of the brain. The probe was moved  
1049 towards the surface of the OB, whilst being observed through a surgical microscope. Once  
1050 the probe was in contact with the surface, but had not entered the brain, the  
1051 manipulator's Z position was set to zero. The signal from the probe was streamed through  
1052 OpenEphys acquisition board and software (OpenEphys, RI, USA). The probe was  
1053 inserted at < 4 μm/s until the number and amplitudes of spikes began to decrease on  
1054 deeper channels, indicating the tip of the probe was exiting the MC layer. This was found  
1055 to be between 400-600 μm from the surface of the OB. From here, the probe was left for  
1056 10 minutes for neural activity to stabilise before recording began.

1057

1058 *Odour stimulation*

1059 Odours were presented using an 8-channel version of the high-speed odour delivery  
1060 device, 4 of which contained odours (A: ethyl butyrate, B: 2-hexanone, C: isoamyl acetate,  
1061 D: eucalyptol) and 4 contained blank (mineral oil) which were used to compensate for  
1062 flow changes. Trials either paired A and B or C and D together. Stimuli were repeated 64  
1063 times and had an 8 s inter-trial interval. Onset of odour was recorded using TTL pulses  
1064 passed through additional channels in the OpenEphys acquisition board. Trial starts were  
1065 triggered on inhalation as detected by the flowmeter.

1066

1067 *Data analysis*

1068 Spikes were sorted using Kilosort2 ([github.com/MouseLand/Kilosort2](https://github.com/MouseLand/Kilosort2);<sup>48</sup>) and classified  
1069 as 'good' when they displayed a strong refractory period visible in their auto-  
1070 correlogram, a typical waveform and a stable firing rate, as 'MUA' (multi-unit activity) if

1071 they presented a typical waveform but a weak refractory period, or 'noise' if they were  
1072 suspected of being electrical or mechanical interference. For a first-pass analysis units  
1073 were classified as "differentially responding" to correlated and anti-correlated stimuli if  
1074 units were found to have significantly ( $p < 0.01$ , Mann Whitney u test) different spike time  
1075 distributions during 4 s post odour onset. However, the cut-off for such distinction will  
1076 always be somewhat arbitrary. For the majority of the analysis, we therefore pooled *all*  
1077 good units across experiments in a pseudo-population. All classifiers used for unit  
1078 recording analysis were support vector machines (SVMs) with linear kernels with a low  
1079 regularisation parameter, which translates to a greater freedom for a classifier to vary  
1080 weights for any given component. Data was split into training and test sets prior to  
1081 classification. Test sets either consisted of 26 trials (summed spike classifiers for  
1082 correlated vs. anti-correlated) or 2 trials (PCA classifiers and short odour pulse  
1083 combinations). Data passed to the summed spike classifiers was pre-processed in one of  
1084 two ways prior to classification.

1085 Firstly, a rolling sum of detected spikes, within variable window sizes was used. The  
1086 window sizes varied from 10 ms to 2000 ms. In addition to window size, window starts  
1087 were also varied. Each window size was trialled with every possible window start from  
1088 zero to four seconds minus the window size from odour onset, with 10 ms incremental  
1089 changes. For example, a 500 ms window was tested with starts varying from 0 to 3500  
1090 ms from odour onset.

1091 Secondly, the coefficients of PCs for units in each trial was used for classification. The PCs  
1092 were found by applying PCA across all units and all training trials. Each PC represented a  
1093 time series and hence the coefficients signify the strength at which that time series was  
1094 followed by a given unit for a given trial. The two holdout trials were not used to find the  
1095 PCs but were then projected onto them and their coefficients used as the test for the  
1096 classifiers. All classifiers were repeated 1000 times with a random selection of holdout  
1097 trials each time.

1098 Finally, for the short odour pulse classification, classifiers were trained on summed  
1099 spikes in windows of 500 ms post odour onset. Each classifier was trained on all but two  
1100 hold out trials. To account for a varying number of trials between animals, training data  
1101 was bootstrapped to 1000 trials of each type. Each trial was randomly selected from the  
1102 initial pool of training trials, and each unit was bootstrapped independently. These  
1103 classifiers were tested on the initial two hold out trials. This was repeated 1000 times  
1104 with different bootstrapped datasets and different hold out trials.

1105 Training data for all classifiers was scaled such that each feature (unit spike count / PC  
1106 coefficient) had a mean value of zero, and a standard deviation of one using the following  
1107 equation:

$$1108 z = \frac{(x - u)}{s}$$

1109 where  $x$  is the initial value of the feature,  $u$  is the mean,  $s$  is the standard deviation, and  $z$   
1110 is the scaled value. Means and standard deviations were calculated using the training data  
1111 so no information from the testing data could influence the scaling. The testing data was

1112 scaled using the same values as for the training. Scaling was applied during every repeat  
1113 in this manner.

1114 **Whole-cell patch recordings**

1115 Whole-cell recordings were performed as described previously<sup>38,49</sup>. Borosilicate pipettes  
1116 (2 x 1.5 mm) were pulled and filled with (in mM) KMeSO3 (130), HEPES (10), KCl (7),  
1117 ATP-Na2 (2), ATP-Mg (2), GTP-Nax (0.5), EGTA (0.05) (pH = 7.3, osmolarity ~290  
1118 mOsm/kg). The OB surface was submerged with ACSF containing (in mM) NaCl (135),  
1119 KCl (5.4), HEPES (5), MgCl2 (1), CaCl2 (1.8), (pH = 7.4 and ~300 mOsm/kg. Signals were  
1120 amplified and low-pass filtered at 10 kHz using an Axoclamp 2B amplifier (Molecular  
1121 Devices) and digitized at 40 kHz using a Micro 1401 analogue to digital converter  
1122 (Cambridge Electronic Design).

1123 After zeroing the pipette tip position at the OB surface, the tip was advanced to reach a  
1124 depth of ~200  $\mu$ m from the surface. Whole-cell patch-clamp recordings were obtained as  
1125 described in<sup>50</sup>. Series resistance was compensated and monitored continuously during  
1126 recording. Neurons showing series resistance >25 M $\Omega$  were discarded from further  
1127 analysis. To estimate the input resistance, a -50 pA current step was delivered at the start  
1128 and end of each recording.

1129 The vertical depth of recorded neurons was calculated as the vertical distance from the  
1130 brain surface. Respiration was recorded using a mass flow sensor (A3100, Honeywell, NC,  
1131 USA) and digitized at 10 kHz. Odours were prepared and delivered as described above  
1132 and triggered to the beginning of inhalation.

1133

1134 *Data analysis*

1135 *Change in membrane potential*

1136 Recordings were spike-clipped using a custom script written in Spike2 (Cambridge  
1137 Electronic Design) and analysed in MATLAB (Mathworks, USA). All recordings were  
1138 baseline subtracted as described previously<sup>51</sup>. The average change in membrane  
1139 potential was defined as the difference between the average membrane potential over a  
1140 2 s period before odour onset and the average membrane potential in the first 500 ms  
1141 (~2 sniffs) after odour onset.

1142

1143 *Change in spike frequency*

1144 Action potentials were counted from raw traces, converted into spike frequency in 50 ms  
1145 bins and plotted as peri-stimulus time histograms (PSTH). The net change in spike  
1146 frequency was defined as the difference of the average spike frequency during 2 s before  
1147 onset and 500 ms after onset.

1148

1149 *Arithmetic sum*

1150 Baseline-subtracted traces obtained from independent component odour (A and B)  
1151 presentations were either summed and averaged in an in-phase manner to generate the  
1152 arithmetic sum equivalent of the correlated response or phase-shifted to generate the  
1153 equivalent of the anti-correlated response.

1154  
1155  
1156  
1157  
1158  
1159

$$\begin{aligned} \text{Arithmetic sum}(\text{correlated}) &= (Vm_{\text{odourA}} + Vm_{\text{odourB}})/2 \\ \text{Arithmetic sum}(\text{anticorrelated}) \\ &= (Vm_{\text{odourA}} + \text{shifted } Vm_{\text{odourB}} + \text{shifted } Vm_{\text{odourA}} + Vm_{\text{odourB}})/4 \end{aligned}$$

1160 **Dual-energy fast photoionisation detection (defPID, [Supplementary Methods Fig. 2](#))**  
1161

1162 Two photoionisation detectors (200B miniPID, Aurora Scientific, Aurora ON, Canada)  
1163 fitted with UV lamps of emission energy 10.6 eV (PID high) and 8.4 eV (PID low) were  
1164 used to discriminate ethyl butyrate (EB, ionisation energy = 9.9 eV) from  $\alpha$ -Terpinene  
1165 (AT, ionisation energy = 7.6 eV) or ethyl valerate (EV, ionisation energy = 10.0 eV) from  
1166 tripropyl amine (TA, ionisation energy = 7.2 eV). To accommodate the lower voltage UV  
1167 lamp, resonance circuitry in the PID headstage electronics was adjusted according to  
1168 manufacturer's recommendations. Specifically, potentiometer 'PT1' was adjusted up to  
1169 the point where the 8.4 eV lamp began to glow. Further, we tested if the now converted  
1170 PID low was now sensitive to only AT and TA while not detecting EB and EV. The PID  
1171 inlets were connected with a 3-way connector to detect incoming odours by both PIDs  
1172 simultaneously from a common point. PID heads were held on lab stands with the PID  
1173 inlet at approximately 4 cm above ground level.

1174

1175 *Odour delivery*

1176 Odours were held in ceramic crucibles (5 cm diameter, 6 ml volume) covered in an air-  
1177 tight fashion using glass lids. Odours were released for 5 s with an inter-trial interval of  
1178 15 s by Arduino-based robots programmed to lift the lids from the crucibles using a servo  
1179 motor (TowerPro SG-5010, Adafruit, UK). Lid lifting events were triggered by the Arduino  
1180 board, recorded in Spike2 and defined as the onset of odour for analysis. Both the Arduino  
1181 board and Spike2 were controlled by a portable computer and used the same clock for  
1182 synchronisation. Experiments were carried out in a large open space, both indoors and  
1183 outdoors ([Supplementary Methods Fig. 2f,g](#)).

1184 *Outdoors setup:* PIDs and odour delivery system as described above were used to record  
1185 for multiple trials in different conditions on a day with low wind ( $\sim$ 8-12 mph  $\approx$  3-5 m/s,  
1186 recorded with a 2-axis ultrasonic wind sensor (Gill Instruments, Hampshire, UK)).  
1187 Outdoor experiments were performed on a  $\sim$ 6 m x 10 m wooden patio structure  
1188 surrounded by trees. Measurement of odour correlations in the outdoor setting were  
1189 complicated by the presence of background odours: If background odours are detectable  
1190 by both PIDs, measured correlation will be artificially inflated; if they can be ionized only  
1191 by the "PIDhigh" they will artificially decrease the measured correlation.

1192 *Indoors setup:* A digitally controlled fan (2214F/2TDH0, ebm-papst, Chelmsford, UK) was  
1193 placed at a distance of 325 cm facing the PID inlet. An exhaust line was situated behind  
1194 the PID inlet to ensure the direction of air from the fan towards the PID inlet. During a  
1195 recording, the fan was set to maximum speed such that it pushed approximately 550

1196 cf/min (cubic feet per minute,  $\approx 260 \text{ l/s}$ ) of air towards the PID inlet. A 25x25x25 cm  
1197 Thermocool box was placed 200 cm downwind of the fan acting as an obstacle to air  
1198 movement, promoting complex air movement patterns at the PID inlet. The pump at each  
1199 PID was set to  $\approx 0.02 \text{ l/s}$  suction speed, unlikely to perturb overall airflow dynamics  
1200 substantially.

1201

1202 *Recording conditions*

1203 6 ml of the desired odour(s) were filled in two crucibles and placed in different locations  
1204 based on the experimental conditions as described below:

1205

1206 1. Low energy only: The 'low-energy odour' (AT or TA) was placed 40 cm (radial distance  
1207 d) away from the PID inlet, and displaced either 25 cm left or 25 cm right of the midline  
1208 (the line between the PID inlet and the centre of the fan). The odour source was alternated  
1209 between left and right positioning relative to the midline to remove any possible bias  
1210 from positioning in the air stream. The purpose of this recording condition was to  
1211 generate data to calculate the linear transformation from the low energy signal to the  
1212 high energy signal ([Supplementary Methods Fig. 2c,d](#)).

1213 2. Mix: 3 ml EB + 3 ml AT (or 3 ml EV + 3 ml TA) was pipetted in one crucible and placed  
1214 either 25 cm left or 25 cm right of the midline at radial distances of 20 cm, 40 cm and 60  
1215 cm. The purpose of this recording condition was to determine how the temporal structure  
1216 of individual odours in a plume behaved when the odours were emitted from the same  
1217 source.

1218 3. Separate: 3 ml EB and 3 ml of AT (or 3 ml EV and 3 ml TA) were individually pipetted  
1219 in two different crucibles and placed at a radial distance of 40 cm from the PID inlet. For  
1220 the s=50 cm apart condition, one odour source was placed 25 cm left of the midline while  
1221 the other was 25 cm on the right of the midline and vice-versa (equal number of trials for  
1222 both cases) separating the odour sources by 50 cm. This procedure was repeated for lateral  
1223 distances of s=30 cm and s=10 cm. The '50 cm apart' case was repeated for radial  
1224 distances of d=20 cm and d=60 cm. The purpose of this recording condition was to  
1225 determine how the temporal structure of individual odours in a plume behaved when the  
1226 odours were emitted from separated sources but were still free to mix in air.

1227

1228 *Data analysis*

1229 Decomposition procedure: The low energy odour (AT) was recorded using both PIDs as  
1230 described above. Assuming a linear relation between the recorded signals from the 2  
1231 PIDs, we plotted the recorded events with a linear regression fit ([Supplementary](#)  
1232 [Methods Fig. 2c](#)) and calculated slope and  $R^2$  value of the fit. The scaling factor ( $6.82 \pm$   
1233  $0.356$ , mean  $\pm$  SD) was calculated as the average slope of all linear fits for  $R^2 \geq 0.9$ .  
1234 The 'PID low' traces were multiplied by this scaling factor which was termed 'estimated  
1235 low energy odour' ([Supplementary Methods Fig. 2e](#)). The 'estimated high energy odour'  
1236 was calculated by subtracting the estimated low energy odour from the 'PID high' traces.

1237 Correlation calculation: Custom written scripts in MATLAB (Mathworks, USA) were used  
1238 to calculate the correlation coefficient between the estimated low energy odour and the  
1239 estimated high energy odour for all conditions. Box plots were obtained from these values  
1240 using Igor Pro 6 (WaveMetrics, USA).

1241 **Methods references**

1242 39. Ishii, T., Hirota, J. & Mombaerts, P. Combinatorial coexpression of neural and  
1243 immune multigene families in mouse vomeronasal sensory neurons. *Curr. Biol.* **13**, 394–400 (2003).

1245 40. Haddad, R., Lanjuin, A., *et al.* Olfactory cortical neurons read out a relative time  
1246 code in the olfactory bulb. *Nat. Neurosci.* **16**, 949–957 (2013).

1247 41. Madsen, L., Garner, A. R. R., *et al.* Transgenic Mice for Intersectional Targeting of  
1248 Neural Sensors and Effectors with High Specificity and Performance. *Neuron* **85**,  
1249 942–958 (2015).

1250 42. Raiser, G., Galizia, C. G. & Szyszka, P. A High-Bandwidth Dual-Channel Olfactory  
1251 Stimulator for Studying Temporal Sensitivity of Olfactory Processing. *Chem.*  
1252 *Senses* **42**, 141–151 (2017).

1253 43. Abraham, N. M., Spors, H., *et al.* Maintaining accuracy at the expense of speed:  
1254 Stimulus similarity defines odor discrimination time in mice. *Neuron* **44**, 865–876  
1255 (2004).

1256 44. Wadhwa, N., Rubinstein, M., Durand, F. & Freeman, W. T. Phase-Based Video  
1257 Motion Processing. *ACM Trans. Graph.* **32**, 1–10 (2013).

1258 45. Lopes, G., Bonacchi, N., *et al.* Bonsai: an event-based framework for processing  
1259 and controlling data streams. *Frontiers in Neuroinformatics* vol. 9 7 (2015).

1260 46. Ghatpande, A. S. & Reisert, J. Olfactory receptor neuron responses coding for rapid  
1261 odour sampling. *J. Physiol.* **589**, 2261–2273 (2011).

1262 47. Pachitariu, M., Stringer, C., *et al.* Suite2p: beyond 10,000 neurons with standard  
1263 two-photon microscopy. *bioRxiv* 061507 (2016) doi:10.1101/061507.

1264 48. Pachitariu, M., Steinmetz, N., Kadir, S., Carandini, M. & Harris, K. D. Kilosort:  
1265 realtime spike-sorting for extracellular electrophysiology with hundreds of  
1266 channels. *bioRxiv* 061481 (2016) doi:10.1101/061481.

1267 49. Jordan, R., Fukunaga, I., Kollo, M. & Schaefer, A. T. Active Sampling State  
1268 Dynamically Enhances Olfactory Bulb Odor Representation. *Neuron* **98**, 1214–  
1269 1228 (2018).

1270 50. Margrie, T. W., Brecht, M. & Sakmann, B. In vivo, low-resistance, whole-cell  
1271 recordings from neurons in the anaesthetized and awake mammalian brain.  
1272 *Pflugers Arch. Eur. J. Physiol.* **444**, 491–498 (2002).

1273 51. Abraham, N. M., Egger, V., *et al.* Synaptic Inhibition in the Olfactory Bulb  
1274 Accelerates Odor Discrimination in Mice. *Neuron* **65**, 399–411 (2010).

1275

1276 **Acknowledgements**

1277 We thank the animal facilities at National Institute for Medical Research and the Francis  
1278 Crick Institute for animal care and technical assistance. We thank the mechanical and  
1279 electronic workshops in MPI Heidelberg (N. Neef, K. Schmidt, M. Lukat, R. Roedel, C.  
1280 Kieser) and London (A. Ling, A. Hurst, M. Stopps) for support during development and  
1281 construction, the Aurora Scientific team for suggestions for adapting the miniPID, T.  
1282 Margrie for discussion, Venkatesh Murthy for discussions and suggestions on the OSN  
1283 imaging experiments, and A. Fleischmann, K. Franks, F. Guillemot, M. Hausser, F. Iacaruso,  
1284 R. Jordan, J. Kohl, T. Mrsic-Flogel, V. Pachnis, A. Silver, and P. Znamenskiy for comments  
1285 on earlier versions of the manuscript. We thank the members of the Odor2Action  
1286 NeuroNex network, in particular J. Victor, J. Crimaldi, B. Smith, M. Schmucker, and J.  
1287 Verhagen for discussion. This work was supported by the Francis Crick Institute which  
1288 receives its core funding from Cancer Research UK (FC001153), the UK Medical Research  
1289 Council (FC001153), and the Wellcome Trust (FC001153); by the UK Medical Research  
1290 Council (grant reference MC\_UP\_1202/5); a Wellcome Trust Investigator grant to ATS  
1291 (110174/Z/15/Z), a BIF doctoral fellowship to ACM, and a DFG postdoctoral fellowship  
1292 to TA.

1293 **Author Contributions**

1294 ATS conceived the project, TA, AE, DD, ATS designed experiments with input from ACM,  
1295 TW, JH, and ST; TA (in vivo imaging, plume measurements), AE (plume measurements,  
1296 frequency and correlation behaviour), DD (plume measurements, whole-cell recordings),  
1297 ACM (source separation behaviour), TW (unit recordings), ST (analysis for OSN imaging),  
1298 JH (source separation behaviour) performed experiments and analysed data, IF  
1299 contributed tools and to experimental design, ST performed simulations, TA, AE, ATS  
1300 wrote the manuscript with input from all authors.

1301 **Author Information**

1302 Author Information Reprints and permissions information is available at  
1303 [www.nature.com/reprints](http://www.nature.com/reprints). The authors declare no competing financial interests.  
1304 Readers are welcome to comment on the online version of the paper. Correspondence  
1305 and requests for materials should be addressed to ATS ([andreas.schaefer@crick.ac.uk](mailto:andreas.schaefer@crick.ac.uk)).

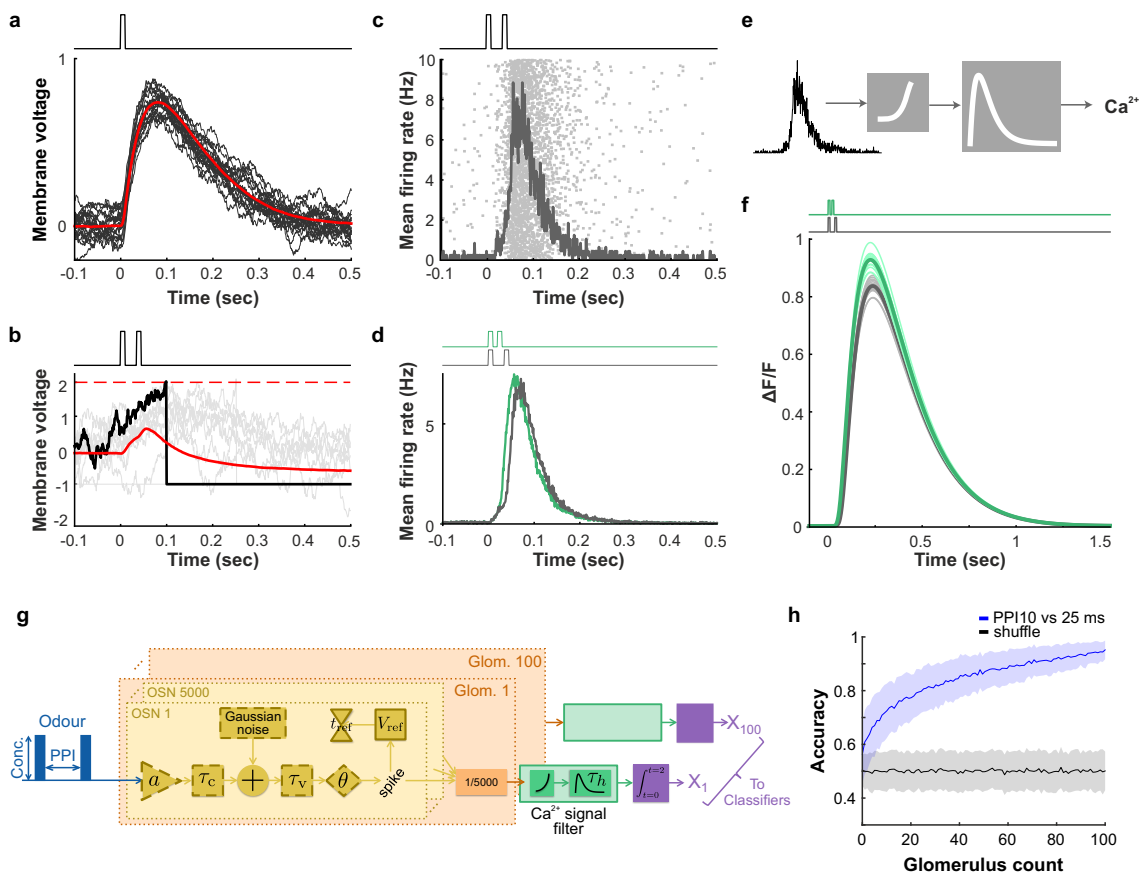
1306 **Data availability**

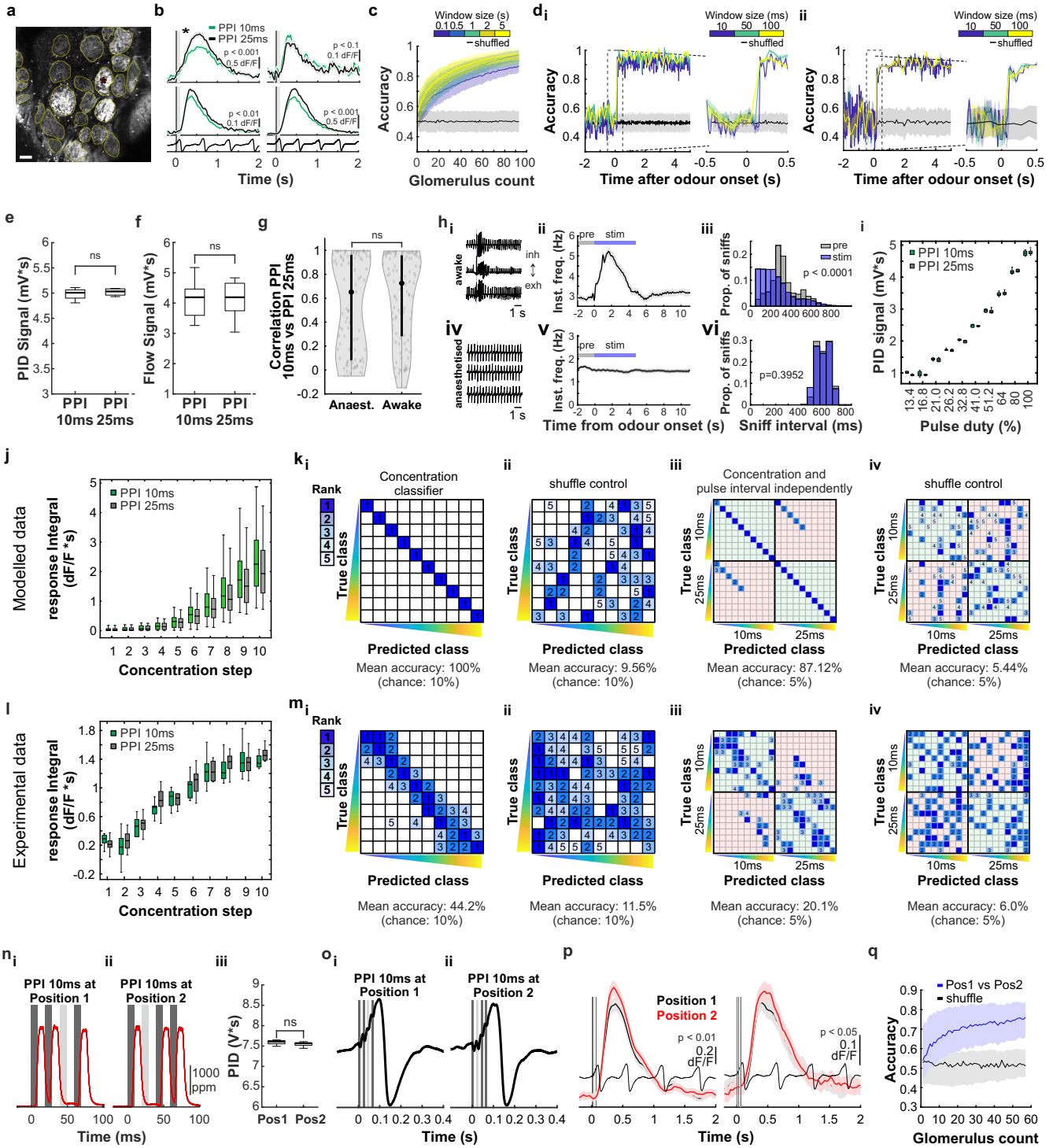
1307 Data related to the OSN model (**Extended Data Fig. 1**) is available at  
1308 <https://github.com/stootoon/crick-osn-model-release>. Data related to the glomerular  
1309 classifier analysis (**Extended Data Fig. 6**) is available at  
1310 <https://github.com/stootoon/crick-osn-decoding-release>. The remaining data that  
1311 support the findings of this study will be made available by the authors upon request.

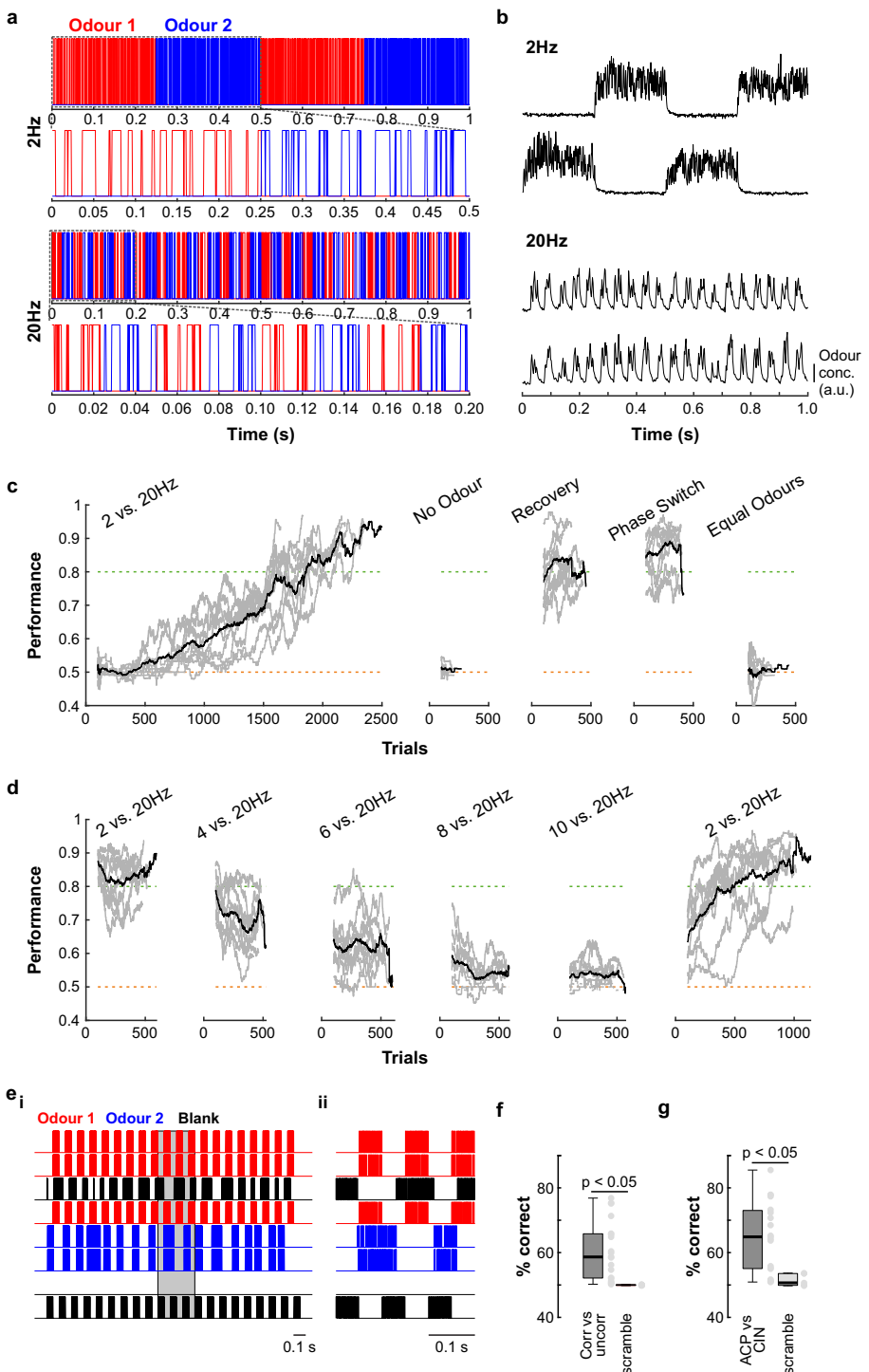
1312 ***Code availability***

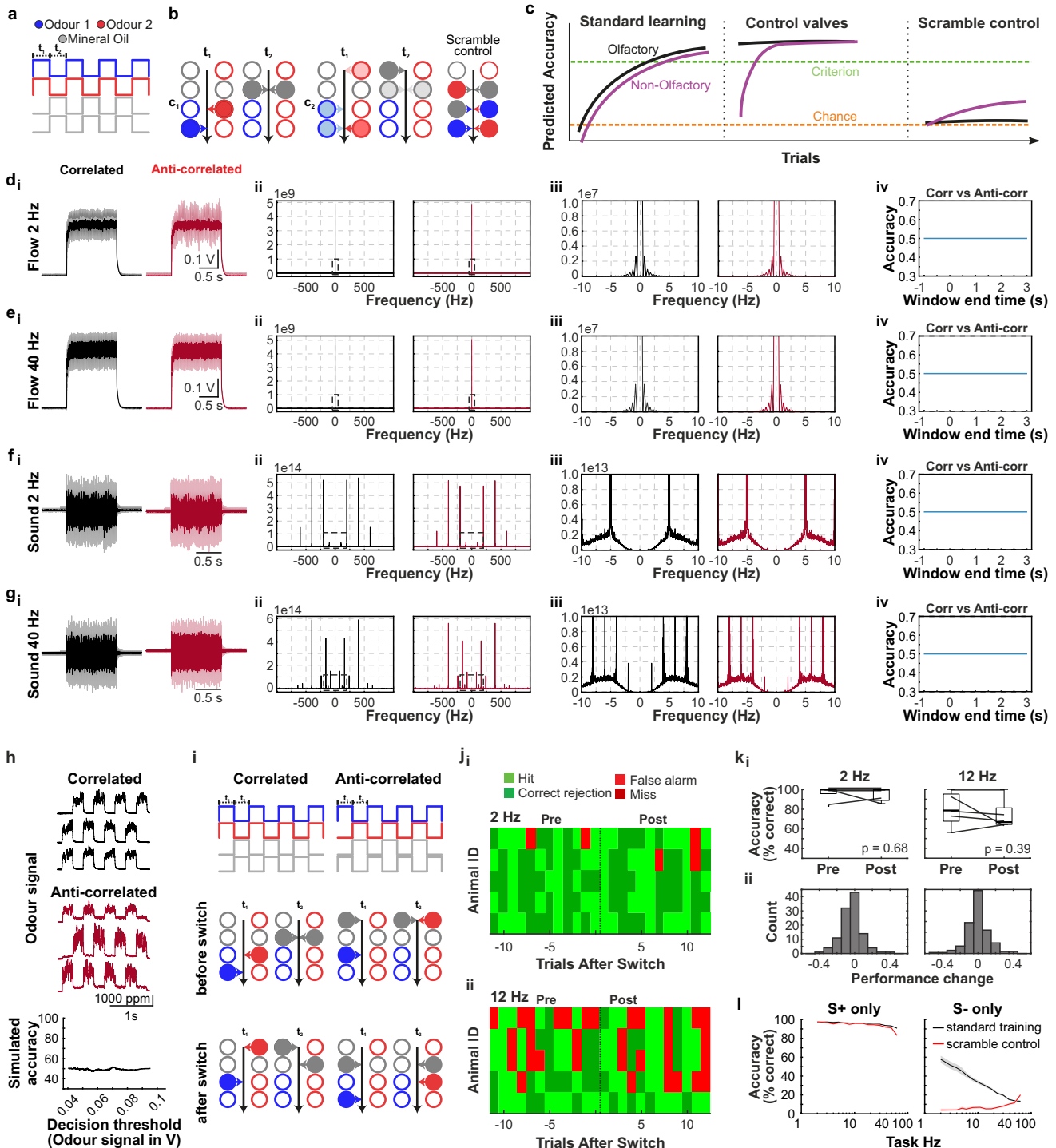
1313 All custom Python scripts to generate pulses (PyPulse, PulseBoy) are available at  
1314 <http://github.com/RoboDoig> and <http://github.com/warnerwarner>. Code for  
1315 controlling AutonoMouse is available at  
1316 [https://figshare.com/articles/AutonoMouse\\_Code/ 7616090](https://figshare.com/articles/AutonoMouse_Code/7616090). Code related to the OSN  
1317 model is available at <https://github.com/stootoon/crick-osn-model-release>. Code  
1318 related to the glomerular classifier analysis is available at  
1319 <https://github.com/stootoon/crick-osn-decoding-release>.

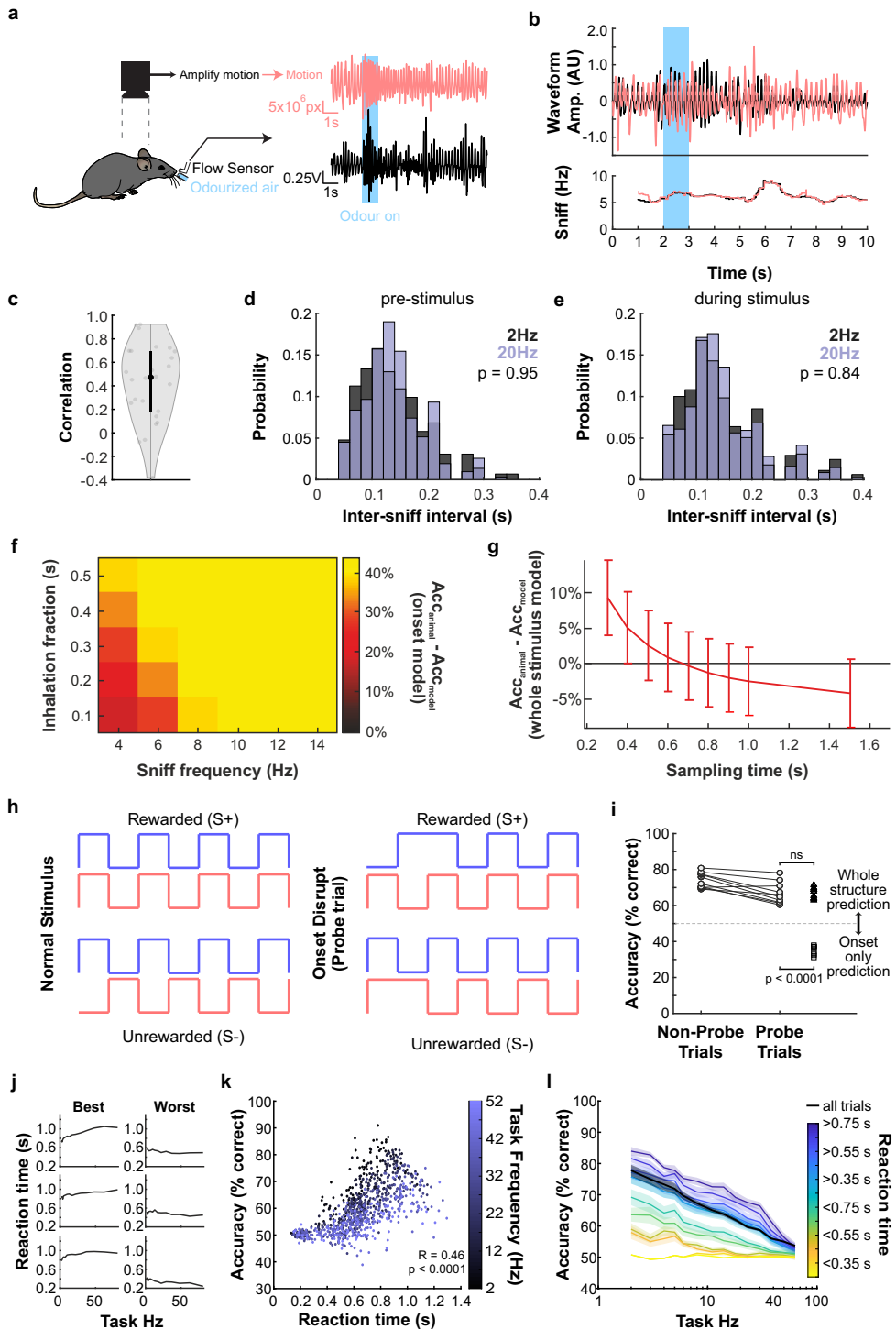
1320

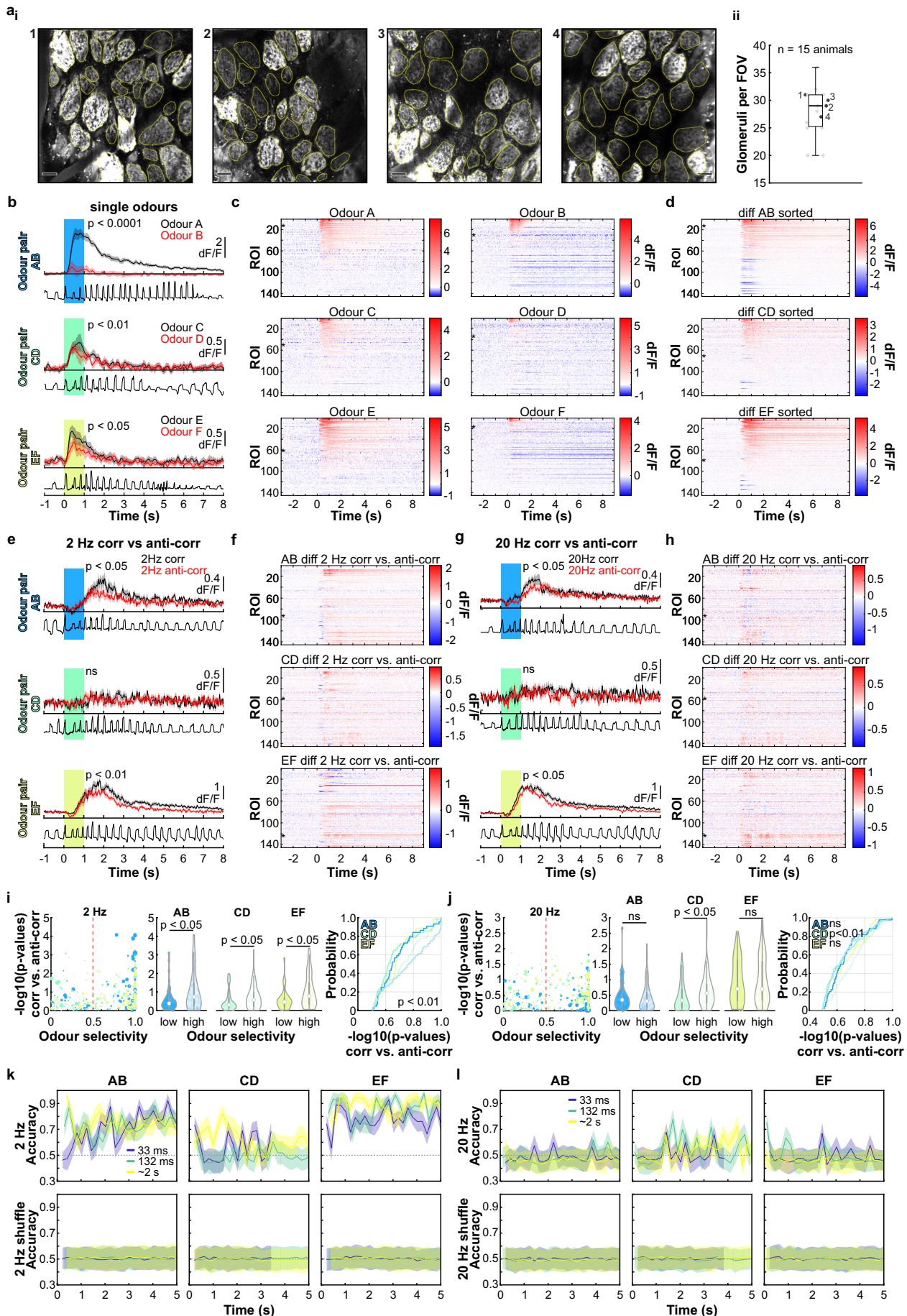


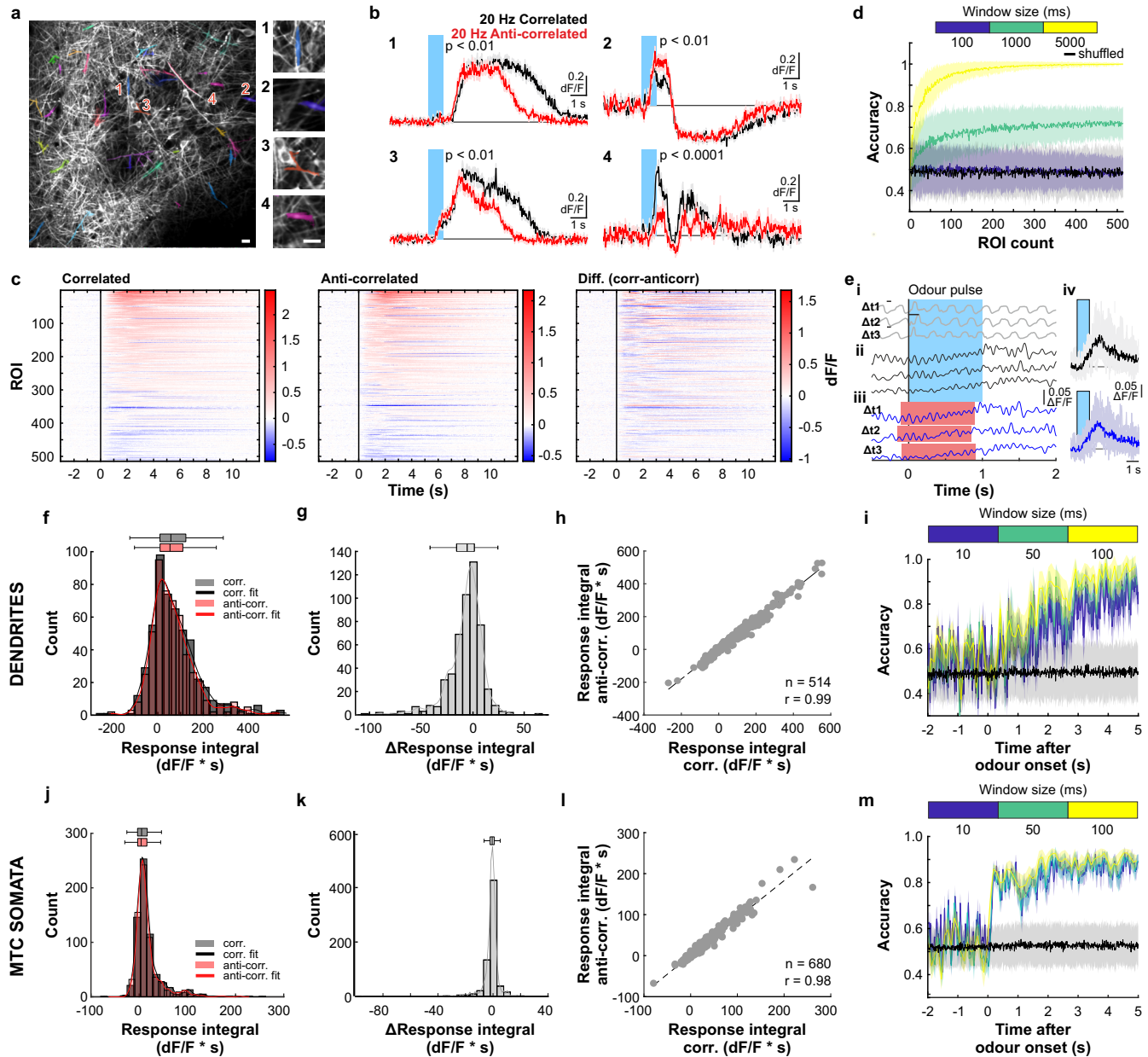


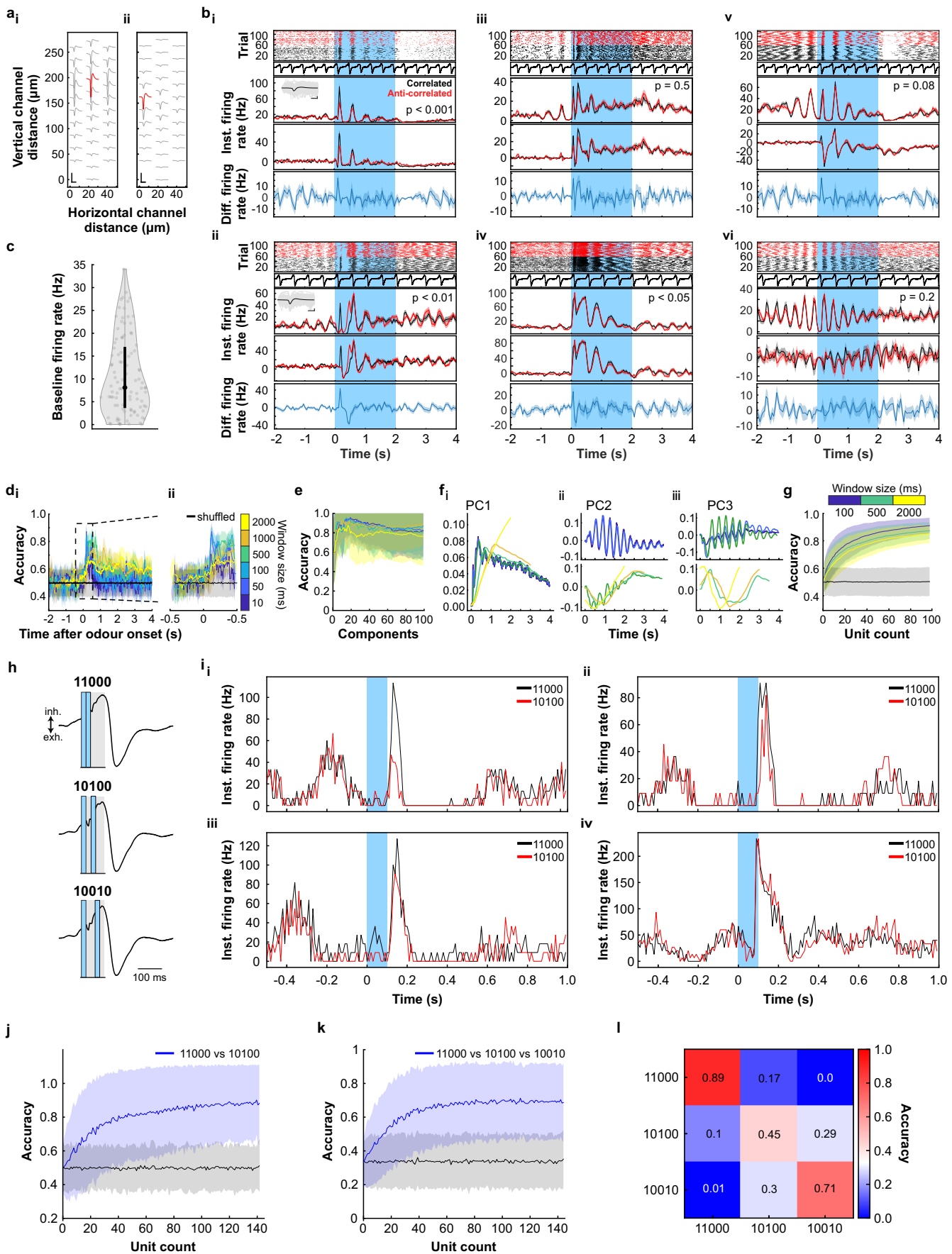


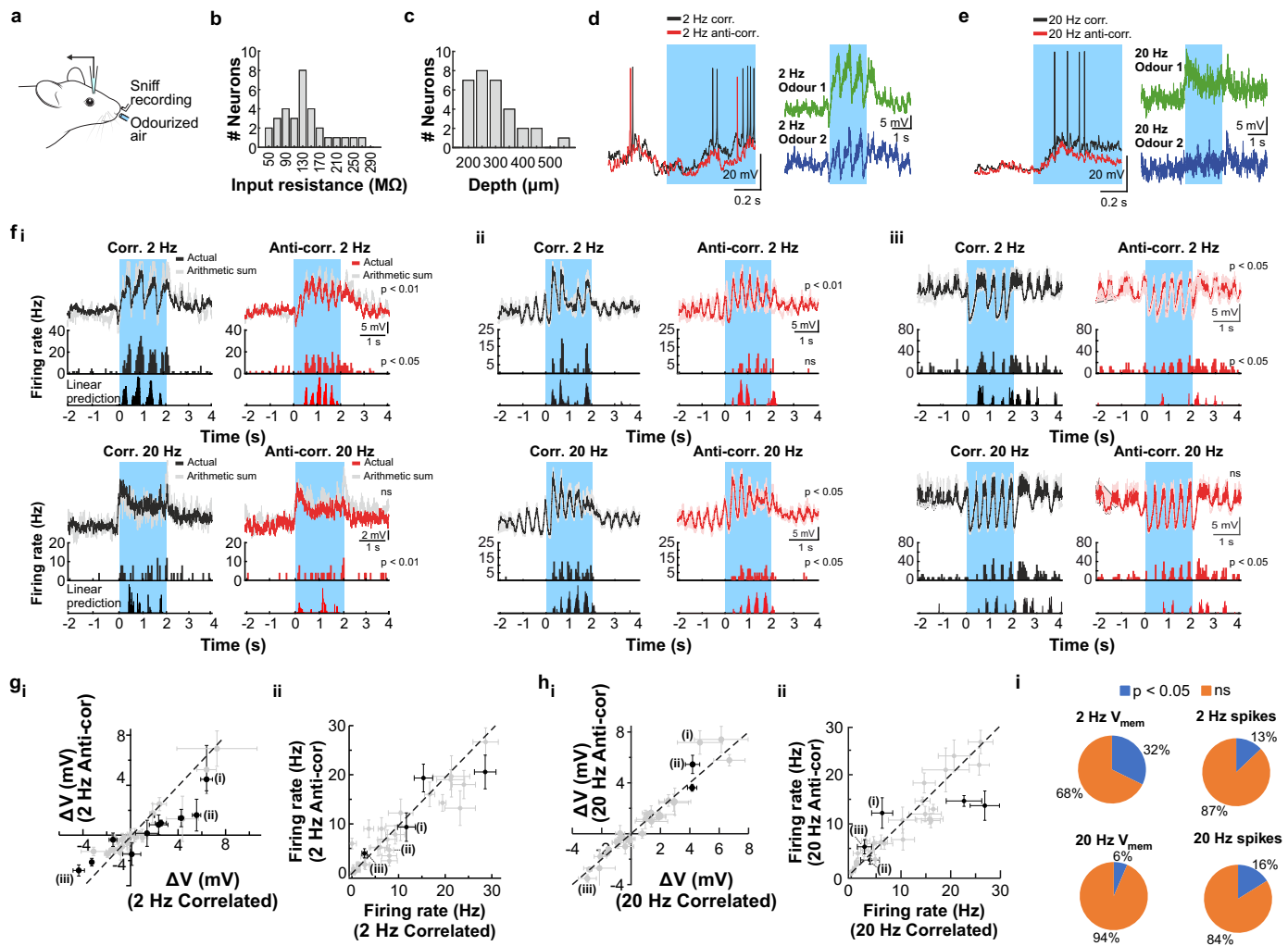


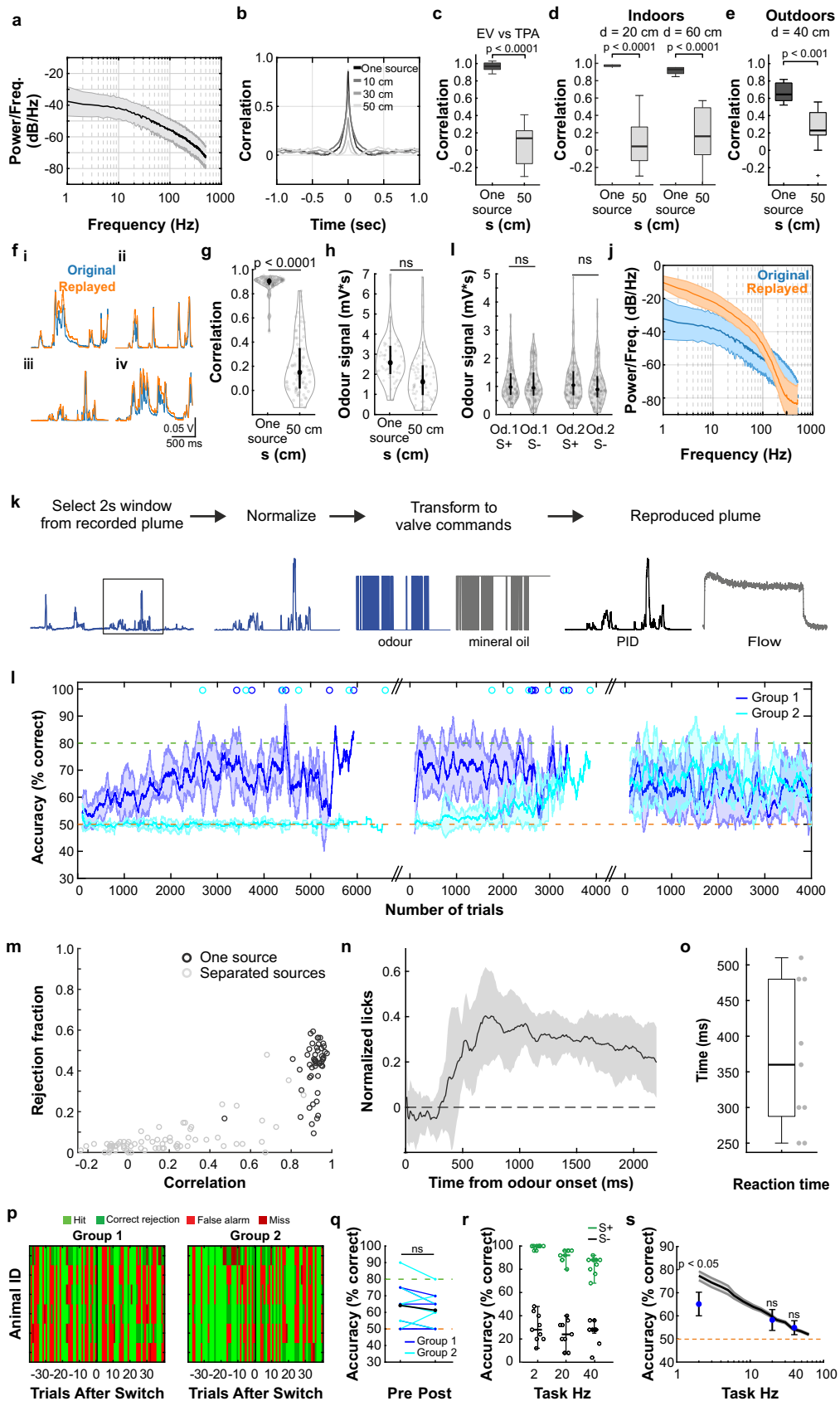












1321 **Extended Data Fig. 1 | Distinguishing fast odour stimuli with slow OSNs.**  
1322 **a**, Membrane voltage relative to baseline of a single model OSN in response to a 10 ms  
1323 odour pulse. Black traces are individual trials; red trace is average over 20 trials. OSN  
1324 spike threshold has been set high enough to prevent spiking to illustrate the subthreshold  
1325 voltage time course. **b**, Membrane voltages (grey traces) of ten OSNs from a population of  
1326 5000 in response to a paired odour pulse with pulse width 10 ms and PPI of 25 ms. The  
1327 voltage time course for one example OSN is in black. Several OSNs reach the OSN spike  
1328 threshold (dashed red line) and are temporarily reset to the refractory voltage of -1. The  
1329 population average membrane voltage (red) reveals membrane charging in response to  
1330 odour stimulation and the subsequent discharging and refractory period. **c**, Raster  
1331 showing the spike times (dots) of the full population from **b** and the corresponding mean  
1332 firing rate (trace) estimated in 1 ms bins. **d**, Mean firing rates computed over 20 trials in  
1333 response to paired odour pulses of width 10 ms and PPIs of 10 ms (green) and 25 ms  
1334 (black). **e**, Model calcium signals are produced by squaring the instantaneous mean firing  
1335 rate and filtering the result with a calcium imaging kernel. **f**, Model calcium responses to  
1336 the paired odour stimulus with a PPI of 10 ms (green) and 25 ms (black). Thin traces are  
1337 single trials, thick traces are averages over 15 trials. **g**, Schematic of the OSN model.  
1338 Variables in dashed bounding boxes are changed for each glomerulus (see Methods). **h**,  
1339 Linear classifier analysis over an increasing subset size of glomeruli (1-100; plotted is  
1340 mean  $\pm$  SD, 256 repeats for random subsets of n glomeruli generating 256 unshuffled and  
1341 256 shuffled accuracies).

1342 **Extended Data Fig. 2 | Sub-sniff odour information in the olfactory bulb input layer.**  
1343 **a**, GCaMP6f fluorescence recorded in olfactory bulb glomeruli in an anaesthetised OMP-  
1344 cre:Rosa-GCaMP6f mouse (maximum projection of 8200 frames, glomerulus marked with  
1345 red asterisk corresponds to first example trace shown in **b**). Scale bar: 50  $\mu$ m. **b**, Example  
1346 calcium traces in response to 10 and 25 ms PPI odour stimuli (mean of 50 trials  $\pm$  SEM).  
1347 Bottom: Example respiration traces. P-values derived from unpaired two-sided t-tests  
1348 comparing responses of individual trials integrated over 2 s windows to paired odour  
1349 pulse stimulation. **c**, Classifier accuracy over an increasing number of glomeruli when a  
1350 linear classifier was trained on several response windows (colour-coded black: shuffle  
1351 control) to PPI 10 vs. 25 ms stimuli (mean  $\pm$  SD of up to 93 glomeruli from 4 individual  
1352 animals; 500 repetitions). **d<sub>i</sub>**, Classifier accuracy when trained on all glomeruli in  
1353 response to PPI 10 vs. 25 ms stimuli recorded in anaesthetised animals (n = 93 glomeruli,  
1354 mean  $\pm$  SD from 4 individual animals) with a sliding window of different durations  
1355 (colour-coded; black: shuffle control; 100 repetitions) starting at 2 s before odour onset  
1356 (left) and time period between -0.5 and 0.5 s from odour onset shown at higher  
1357 magnification (right). **d<sub>ii</sub>**, Same as **d<sub>i</sub>** for awake animals (n = 100 glomeruli, mean  $\pm$  SD  
1358 from 5 individual animals). **e**, Odour and **f**, flow signal integrated over 2 s for PPI 10 ms  
1359 and PPI 25 ms stimuli (10 repeats each, odour: p = 0.1841, flow: p = 0.1786, unpaired  
1360 two-sided t-test). **g**, Correlation coefficients of glomerular calcium responses to PPI 10 vs.  
1361 25 ms in anaesthetised (n = 93 glomeruli from 4 individual animals) and awake (n = 100  
1362 glomeruli from 5 individual animals) mice (p = 0.3187, unpaired two-sided t-test,  
1363 measured as in Fig. 1 from OMP-Cre:Rosa-GCaMP6f mice). Violin plots show the median

1364 as a black dot and the first and third quartile by the bounds of the black bar. **h<sub>i</sub>**, Example  
1365 respiration traces recorded using a flow sensor from awake mice. Inhalation goes in the  
1366 upwards, exhalation in the downwards direction. **h<sub>ii</sub>**, Average instantaneous sniff  
1367 frequency from one example animal plotted as a function of time (n = 24 trials, mean  $\pm$   
1368 SEM). The odour stimulus consisted of two 10 ms long odour pulses either 10 or 25 ms  
1369 apart (see Fig. 1c). **h<sub>iii</sub>**, Distribution of sniff intervals during a 2 s window before (grey)  
1370 and a 5 s window after (blue) odour stimulus onset ( $p = 1.02\text{e-}189$ , two-sample  
1371 Kolmogorov-Smirnov test). **h<sub>iv-vi</sub>**, Same but for the anaesthetised condition ( $p = 0.3952$ ,  
1372 two-sample Kolmogorov-Smirnov test). **i**, Mean odour signal for PPI 10 and 25 ms for 10  
1373 increasing concentration steps defined by modulating valve pulse duty (see Methods and  
1374 Supplementary Methods Fig. 1). There were no significant differences in odour  
1375 concentration between both stimuli (unpaired two-sided t-tests). **j**, Modelled response  
1376 integrals to PPI 10 vs. 25 ms stimulations over a 10-fold concentration range pooled over  
1377 all 20 trials and 100 glomeruli (see Methods). Box plots show median and extend from  
1378 the 25<sup>th</sup> to 75<sup>th</sup> percentiles, whiskers extend to the 5<sup>th</sup> and 95<sup>th</sup> percentiles. **k<sub>i</sub>**, Confusion  
1379 matrix of support vector machine (SVM)-based classification results of modelled  
1380 glomerular signals in response to a range of 10 odour concentrations ranked and colour-  
1381 coded (n = 100 glomeruli). **k<sub>ii</sub>**, Shuffle control with labels assigned randomly. **k<sub>iii</sub>**,  
1382 Confusion matrix showing the ranked and colour-coded results of glomerular responses  
1383 independently classified for 10 ms vs. 25 ms PPI and across the range of 10 odour  
1384 concentrations. **k<sub>iv</sub>**, Shuffle control for **k<sub>iii</sub>** with labels assigned randomly. **l**, Same as **j** but  
1385 2 s response integrals are derived from  $\text{Ca}^{2+}$  imaging data (10 repeats for each  
1386 concentration). **m**, Same as **k** for  $\text{Ca}^{2+}$  imaging data (n = 57 glomeruli, from 2 individual  
1387 animals, 10 repeats for each concentration). Note that 10 ms PPI could be reliably  
1388 distinguished from 25 ms PPI with only few instances where a response to e.g. a 10 ms  
1389 PPI stimulus was misclassified as 25 ms or vice versa (compare light red quadrants to  
1390 light green quadrants). **n**, Shifting the position of 10 ms PPI within a single inhalation. **n<sub>i</sub>**,  
1391 PPI 10 ms at Position 1 or **n<sub>ii</sub>**, at Position 2 of three 10 ms odour pulses. Odour pulses as  
1392 recorded with a PID shown in red, valve commands are shown in dark grey. Light grey  
1393 area shows additional compensatory blank valve command to keep the flow profile  
1394 indistinguishable between stimuli. **n<sub>iii</sub>**, Total odour concentration was independent of the  
1395 pulse profile (10 repeats,  $p = 0.57$ , unpaired two-sided t-test). **o**, Both the 10 ms PPI at  
1396 Position 1 (**o<sub>i</sub>**) and at Position 2 (**o<sub>ii</sub>**) are presented during the inhalation phase  
1397 (respiration shown in black, inhalation upwards, exhalation downwards). **p**, Example  
1398 calcium traces in response to 10 ms PPI at Position 1 (black) and Position 2 (red), shown  
1399 is the mean of 10 trials  $\pm$  SEM. P-values derived from unpaired t-tests comparing 2 s  
1400 integrated responses of individual trials to odour pulses. **q**, Classifier accuracy over  
1401 increasing number of glomeruli when a linear classifier was trained on the 2 s response  
1402 to PPI 10 ms at Position 1 vs. Position 2 (mean  $\pm$  SD of up to 57 glomeruli, from 2  
1403 individual animals, 500 repetitions; blue: PPI 10 ms at Position 1 vs. Position 2, black:  
1404 shuffle control). Boxes in **e,f,n<sub>iii</sub>** indicate 25<sup>th</sup>–75<sup>th</sup> percentiles, thick line is median,  
1405 whiskers are most extreme data points not considered outliers (see Methods).

1406 **Extended Data Fig. 3 | Frequency discrimination experiments.** **a**, Frequency  
1407 discrimination stimuli are produced by alternating presentation of two odours to  
1408 generate a desired odour change frequency. During odour delivery, valves are not held

open but rather randomly opened and closed over time to produce slight variation in odour amplitude for each pulse. This means that odour concentration cannot be used as a cue to learn the task and odour switching frequency is the primary stimulus signal. Furthermore, valve clicking is randomised to minimize any acoustic cues. **b**, Replacing one odour channel with blank, un-odourised air and recording the frequency stimuli with a PID reveals that the desired odour pulse frequency is being produced. **c**, Mice readily learn to discriminate 2 vs. 20 Hz pulse frequency stimuli in a go/no-go task. Replacing the odours with blank channels results in chance-level performance (No odour), which recovers when odours are replaced (Recovery) showing that mice were likely discriminating the odour switching frequency rather than any extraneous cues such as valve noise. The order of odour presentation in the stimuli had no effect on behaviour as when it was shifted (Phase switch) no decrease in performance was observed. Additionally, performance was dependent on the alternation between *different* odours as when the experiment was repeated with the same odours in each channel (Equal odours) performance was at chance level. **d**, To determine the perceptual limit of frequency discrimination, the floor frequency used in the task over successive experiments was increased such that the difference in frequency between the stimuli progressively narrowed. Overall performance decreased as the difference in frequency grew smaller, reaching near-chance level with a frequency difference of 10 Hz (10 vs. 20 Hz). Switching back to the original discrimination (2 vs. 20 Hz) recovered performance quickly, showing that the drop in discrimination ability was truly due to the frequency difference rather than general deterioration of performance over time. **e**, Example uncorrelated stimuli. Combinations of odour 1 (red) and odour 2 (blue) valves are opened with temporal offsets and randomised pulse timing resulting in a correlation of 0 (see Methods). Blank (black) valves are used to keep total airflow constant throughout the stimulus. **e<sub>ii</sub>**, Higher magnification of the area in **e<sub>i</sub>** marked in grey. **f**, Animals show similar average accuracy as shown in Fig. 2k when probed to discriminate correlated from uncorrelated odour pulses at 10 Hz ( $n = 19$  mice, mean  $\pm$  SEM of average accuracy =  $0.6506 \pm 0.0016$ ; after scrambling stimulus identity:  $0.4997 \pm 0.0032$ ;  $p = 0.0175$ , unpaired two-sided t-test). **g**, Animals show similar average accuracy when discriminating the correlation structure of a different odour pair (Acetophenone vs. Cineol) at 10 Hz ( $n = 19$  mice, mean  $\pm$  SEM of average accuracy =  $0.6558 \pm 0.0026$ ; after scrambling stimulus identity:  $0.5165 \pm 0.0048$ ;  $p = 0.0129$ , unpaired two-sided t-test). Grey dots mark average performance of individual animals. Boxes in **f,g** indicate 25<sup>th</sup> – 75<sup>th</sup> percentiles, thick line is median, whiskers are most extreme data points not considered outliers (see Methods).

**Extended Data Fig. 4 | AutonoMouse stimulus and experimental design.** **a**, Detailed schematic of stimulus production; odour presentation (Odour 1: blue, Odour 2: red) is always offset by clean air (Mineral Oil: grey) valves at the same flow levels, to ensure that total flow during the stimulus is constant. **b**, Schematic of the use of valve subsets to produce the desired stimulus.  $t_1$  and  $t_2$  represent valve openings at the corresponding time points shown in **a**. **c<sub>1</sub>** (**b**, left) and **c<sub>2</sub>** (**b**, middle) represent two possible configurations that could be used to produce the same resulting stimulus at the two time

points. Opacity in the colours represents total concentration contribution to the resulting stimulus at the time point. For example, to produce the dual odour pulse at t1, configuration c1 can be used where odour 1 (blue) is delivered from one valve and odour 2 (red) from another valve. During t2 two valves contribute clean air. Alternatively, configuration c2 can be used in which during t1 odour 1 (blue) is generated by 50% opening of two valves, with odour 2 (red) produced by 70% / 30% opening of two other valves respectively. **(b, right)** Scramble control: valve maps (represented by arrow colour) are maintained compared to the training condition but odour vial positions are scrambled resulting in odour stimuli uninformative about reward association whilst maintaining any non-odour cue such as putative sound or flow contributions. **c**, Predicted accuracy for animals in the case that they use solely olfactory temporal correlations (black) and in the case that they use extraneous non-olfactory cues or non-intended olfactory cues (e.g. contaminations, clicking noises) (violet). Note that when switching stimulus preparations to a new set of valves (as in Fig. 2i and below in **i-k**), such non-intended cues would not provide any information about stimulus-reward association, thus animals' accuracies would transiently drop back to chance. **d<sub>i</sub>**, Average flow recordings (mean  $\pm$  SD) of 2 Hz correlated (black, n = 75) and anti-correlated (red, n = 70) trials taken from the AutonoMouse odour port. **d<sub>ii</sub>**, Fourier transform of the flow plots from **d<sub>i</sub>**, showing the power of the signal over a range of 1 kHz. **d<sub>iii</sub>** A zoom in over the range of 10 Hz indicated by the dotted box in **d<sub>ii</sub>**. **d<sub>iv</sub>**, Mean accuracy of a series of linear classifiers trained on an increasing window of the integrated signal starting from 1 s before trial shown in **d<sub>i</sub>**. Classifiers were tested on two withheld trials, one correlated and one anti-correlated, and repeated 100 times. **e**, Same as **d** but for 40 Hz trials (n = 69 correlated and n = 72 anti-correlated). **f<sub>i</sub>**, Average audio recording trace (mean  $\pm$  SD) of 2 Hz stimuli using a microphone placed in close proximity to the AutonoMouse odour port. **f<sub>ii</sub>, f<sub>iii</sub>**, Fourier transforms of the audio signal from **f<sub>i</sub>**. Note, whilst there are notable peaks at specific frequencies, these are present in both correlated and anti-correlated trials. **f<sub>iv</sub>**, Accuracy of a series of linear classifiers as shown in **d** but using the modulus of the audio signal. **g**, Same as **f** but for 40 Hz trials. Note, whilst the sound profile and the Fourier transforms are different between 2 and 40 Hz, there is no difference detectable between correlated and anti-correlated trials. **h**, Example traces of odour signal (ethyl butyrate, isoamyl acetate, PID recorded) during correlated (top) and anti-correlated trials (middle). Simulated maximum accuracy based on differences in mean odour signal (bottom). Simulated accuracy was calculated as the fraction of trials correctly identified as correlated / anti-correlated based on a decision threshold set at some level between the minimum and maximum mean signal. Simulated accuracy was calculated for multiple decision thresholds, increasing the decision threshold from minimum odour signal to maximum odour signal in steps of 1/5000<sup>th</sup> of the range between minimum and maximum. **i**, Detailed schematic of correlated (top left) and anti-correlated (top right) stimulus production before (middle) and after (bottom) switching valves. For the switch control, a set of previously unused odour valves is introduced to rule out potential bias towards a specific valve combination when performing the odour correlation discrimination task. **j**, Trial map of 5 representative animals during 2 Hz (**j<sub>i</sub>**) and 12 Hz (**j<sub>ii</sub>**) correlation discrimination tasks before and after introduction of control valves (n = 12 trials pre-, n = 12 trials post-new valve introduction, new valve introduction indicated by black vertical dotted line. Each row corresponds to an animal, each column within the

1497 row represents a trial. Light green: hit, dark green: correct rejection, light red: false alarm,  
1498 dark red: miss. **k<sub>i</sub>**, Boxplots of mean accuracy for animals (n = 5 mice) pre- and post-  
1499 control for 2 Hz (left) and 12 Hz (right). Box indicates 25<sup>th</sup> – 75<sup>th</sup> percentiles, thick line is  
1500 median, whiskers are most extreme data points not considered outliers, see Methods. P-  
1501 values derived from unpaired t-tests. **k<sub>ii</sub>**, Summary histograms of performance change for  
1502 all animals during all “valve switch” control tests (see Methods) indicating that  
1503 discrimination accuracy was based on intended olfactory cues. The five animals showing  
1504 highest performance before the valve switch/bottle change (and thus the largest  
1505 potential to drop in performance) were analysed. **I**, Discrimination accuracy (n = 33  
1506 animals, mean ± SEM) for rewarded S+ (left) and unrewarded S- (right) trials when  
1507 odours were presented using standard training valve configurations (black) and  
1508 scrambled valve identity (red), data from Fig. 2k. Note that frequencies >40 Hz were  
1509 presented predominantly in the last block of the training schedule and reduced licking in  
1510 the control group (decreased S+ performance and increased S- performance) might be  
1511 due to decreased motivation at that point.

1512 **Extended Data Fig. 5 | Respiration recordings, stimulus onset model and reaction**  
1513 **time for correlation discrimination experiments.** **a**, An overhead camera was used to  
1514 image a head-fixed mouse during a sequence of odour presentations. Simultaneously, a  
1515 flow sensor was placed close to one nostril to monitor respiration to establish the validity  
1516 of motion imaging-based respiration recording. Phase-based motion amplification was  
1517 used to magnify motion on the animal’s flank to capture body movements associated with  
1518 respiration. Right: example for simultaneous respiration measurement with motion  
1519 imaging (red) and flow sensor (black; see Methods and Supplementary Video 2). **b**, Three  
1520 further example trials with respiration rate extracted from motion imaging (red) and  
1521 simultaneous flow sensor recording (black). Below: instantaneous sniff frequencies  
1522 calculated from either sensor were tightly correlated. **c**, Correlation between respiration  
1523 traces extracted from motion imaging and respiration captured by flow sensor (n = 26  
1524 trials, 10 s duration each). Violin plot shows the median as a black dot and the first and  
1525 third quartile by the bounds of the black bar. **d**, Probability distributions of inter-sniff  
1526 intervals for odour presentations (isoamyl acetate vs. ethyl butyrate, 2 Hz and 20 Hz) for  
1527 freely moving animals in AutonoMouse before stimulus onset and **e**, during 2 s odour  
1528 stimulation (n = 605 sniffs for 2 Hz and n = 668 for 20 Hz, two-sample Kolmogorov-  
1529 Smirnov test). **f**, Heat map of accuracy difference between a model where animals rely on  
1530 onset information only (see Methods) and actual animal accuracies across a range of sniff  
1531 frequencies and inhalation fractions (n = 10 mice). No matter what assumed sniff  
1532 frequency and inhalation frequency, the “onset model” deviates substantially from the  
1533 accuracy measured in the behavioural experiments (panels h,i). **g**, Difference between a  
1534 model where animals use the entire stimulus structure (see Methods) and actual  
1535 behavioural accuracies across different stimulus sampling times (n = 10 repeats, mean ±  
1536 SD). The “whole stimulus” model accurately describes animal behaviour indicating that  
1537 mice base a decision about the correlation structure of a stimulus not predominantly on  
1538 the onset. Note the different scales in **f** and **g**. **h**, Schematic of experimental stimulus in  
1539 which the first stimulus pulse was disrupted when presented on “probe trials”. Top:

normal stimulus design, bottom: “onset disrupt” stimuli in which the first pulse in a correlated stimulus is disrupted to be anti-correlated; and vice versa for an anti-correlated stimulus. **i**, Animals were trained on standard (non-probe) correlation discrimination stimuli ( $f = 10$  Hz) but onset disrupt (probe) stimuli were presented randomly on probe trials with a 1/10 probability. Accuracy was only slightly degraded on probe trials (mean  $\pm$  SD of accuracy for non-probe trials  $75.8 \pm 4.4\%$ ; for probe trials  $67.8 \pm 6.1\%$ ;  $p = 0.001$ , paired two-sided t-test,  $n = 9$  mice) but did not drop below chance ( $p = 7.3e-06$ , paired t-test). Importantly, accuracy on probe trials was consistent with whole-structure prediction ( $70.3 \pm 3.5\%$ ,  $p = 0.13$ , paired t-test of comparison to probe trials) and differed significantly from the accuracy of onset-only prediction ( $41.6 \pm 1.5\%$ ;  $p = 1.02e-6$ , paired t-test of comparison to probe trials). **j**, Mean reaction time (time from stimulus onset to first lick in S+ trials) plotted as a function of stimulus pulse frequency for the three animals with the best (left) and the worst (right) global accuracy (mean accuracy across all trials). Better performing animals tend to increase their reaction time as stimulus pulse frequency increases. **k**, Scatter plot of mean accuracy vs. mean reaction time for each animal and stimulus pulse frequency condition (averaged over blocks of 100 trials). Points are colour-coded according to stimulus pulse frequency. Accuracy was significantly positively correlated to reaction time, suggesting that mice that sampled a greater portion of the stimulus made more accurate decisions about its correlation structure (Pearson correlation coefficient  $R = 0.49$ ,  $p < 1.1e-112$ ). **l**, Accuracy (mean  $\pm$  SEM) is plotted as in Fig. 2k, but only trial blocks with reaction times above or below a certain threshold (colour code) are included in the analysis. Where only longer reaction times are considered, global performance is higher than the case where only shorter reaction times are included, again suggesting that longer stimulus sampling improves discrimination of odour correlation structure across all stimulus pulse frequencies.

**Extended Data Fig. 6 | OSN imaging in response to correlated vs. anti-correlated odour stimulation.** **a**, Four example fields of view (FOV) recorded from the dorsal olfactory bulb of individual mice. **a<sub>ii</sub>**, Number of individual glomeruli per FOV in all experimental mice ( $n = 15$ ). The number of individually delineated glomeruli ranges from 20-36 with an average of 28 glomeruli per FOV. Labelled data points (1-4) correspond to FOVs shown in **a<sub>i</sub>**. Scale bars: 50  $\mu$ m. Edges of the box are the 25<sup>th</sup> and 75<sup>th</sup> percentiles, the whiskers extend to the most extreme data points not considered as outliers, see Methods. **b**, Example glomerulus response from OMP-Cre:Rosa-GCaMP6f mice to presentation of individual odours plotted pairwise (AB, CD, EF; mean of 6 trials  $\pm$  SEM). Stimulation period (1 s) is indicated by vertical bar (blue, green and yellow). Bottom: Typical example respiration trace. P-values derived from unpaired two-sided t-tests comparing 2 s integrated responses between paired odours. **c**, Averaged calcium transients from all glomeruli ( $n = 145$  from 5 individual animals) in response to individual odours, plotted as colour maps sorted by response magnitude. **d**, Difference between glomerulus responses to individual odours plotted pairwise as colour maps. Glomeruli are sorted by average magnitude of response difference. **e**, Example glomerulus response to presentation of correlated vs. anti-correlated odour pairs fluctuating at 2 Hz (mean of 12 trials  $\pm$  SEM). Bottom: typical example respiration trace.

1583 P-values derived from unpaired two-sided t-tests comparing 2 s integrated responses of  
1584 individual trials to correlated and anti-correlated odour stimulation. **f**, Difference  
1585 between glomerulus responses to 2 Hz correlated and anti-correlated odours as colour  
1586 maps sorted as shown in **d**. **g-h**, Same as in **e-f** but for 20 Hz correlated vs. anti-correlated.  
1587 Example glomerulus from **b,e,g** indicated with an asterisk in colour maps in **c,d,f,h**. **i**, Left:  
1588 P-values derived from comparing trials of the summed 2 s response to correlated vs. anti-  
1589 correlated odour stimulation at 2 Hz (unpaired two-sided t-tests) for three odour pairs  
1590 (colour-coded) as a function of glomerulus selectivity to individual odours ( $n = 145$   
1591 glomeruli). Selectivity is calculated as the difference between the absolute response to  
1592 single odours scaled by the summed absolute response. A threshold is set at 0.5 defining  
1593 glomeruli as low or high selective. Dot size represents magnitude of the summed  
1594 response. Middle: Comparison of p-values between low and high selective glomeruli ( $p <$   
1595 0.05, unpaired two-sided t-test). Violin plots show the median as a white dot and the first  
1596 and third quartile by the bounds of the grey bar. Right: Cumulative distribution function  
1597 of p-values for low and high selective glomeruli ( $p < 0.01$  for all pairwise comparisons,  
1598 two-sample Kolmogorov-Smirnov test). **j**, Same as **i** but for 20 Hz, ( $n = 145$  glomeruli). **k**,  
1599 Top row: Mean  $\pm$  SD over 100 repetitions of classifier accuracy when trained on all  
1600 responsive glomeruli ( $n = 145$  available, from 5 individual animals, see Methods) to  
1601 discriminate 2 Hz correlated vs. anti-correlated stimuli, trained separately for each of the  
1602 three odour pairs and within sliding windows of different widths (colours); x-coordinates  
1603 indicate latest extent of each window. Bottom row: same as top row but with labels  
1604 shuffled as control. **l**, Same as **k** for 20 Hz correlated vs. anti-correlated odours. Some data  
1605 points in **k, l** are absent because not all time points had responsive ROIs for every window  
1606 size (see Methods).

1607 **Extended Data Fig. 7 | Odour correlation structure is encoded in dendrites of**  
1608 **olfactory bulb output neurons.** **a**, GCaMP6f fluorescence from mitral and tufted cells  
1609 and their dendrites recorded in the dorsal portion of the olfactory bulb of a Tbet-  
1610 cre:Rosa-GCaMP6f mouse (maximum projection of 8000 frames). Dendritic ROIs are  
1611 superimposed in colour. Four dendritic segments (1-4) are shown in higher  
1612 magnification, scale bars: 20  $\mu$ m. **b**, Four example calcium traces extracted from dendritic  
1613 segments shown in **a** that show differential response kinetics to correlated (black) and  
1614 anti-correlated (red) stimulation (mean of 24 trials  $\pm$  SEM,  $f = 20$  Hz). In total, 24% of  
1615 dendritic segments showed significantly different integral responses (0-5 s after odour  
1616 onset,  $p < 0.01$ , unpaired two-sided t-test; 121/514) to the two stimuli. **c**, Average calcium  
1617 transients as colour maps for correlated (left) anti-correlated (middle) and the difference  
1618 between both odour stimulations (right) of all analysed dendritic segments ( $n = 514$ , from  
1619 6 individual animals). **d**, Classifier accuracy over an increasing number of dendritic ROIs  
1620 trained on several response windows (colour-coded) to discriminate correlated vs. anti-  
1621 correlated stimuli at 20 Hz ( $n =$  up to 514, mean  $\pm$  SD from 6 individual animals, black:  
1622 shuffle control). **e**, Method of aligning calcium traces to first inhalation after odour  
1623 stimulus onset. **e<sub>i</sub>**, Representative respiration traces recorded using a flow sensor placed  
1624 in front of the nostril contralateral to the imaging window. The first inhalation peaks were  
1625 detected and the time ( $\Delta t$ ) to the first inhalation after odour onset was calculated for each  
1626 trial individually. **e<sub>ii</sub>**, Representative calcium transients in response to a single odour  
1627 presentation (here: 20 Hz correlated). **e<sub>iii</sub>**, Transients are shifted according to  $\Delta t$ . **e<sub>iv</sub>**,

1628 Individual calcium transients (faint colours, 24 trials) in response to 20 Hz correlated  
1629 odour presentations with the average calcium signal (thick traces) superimposed. Top:  
1630 before aligning to first inhalation after odour onset, bottom: after alignment. Blue bar  
1631 represents the odour presentation phase (approximate for the aligned data). **f**,  
1632 Distribution of odour response integrals from all recorded ROIs ( $n = 514$ ) for correlated  
1633 (grey) and anti-correlated (red) stimulation. Box indicates 25<sup>th</sup> – 75<sup>th</sup> percentiles, thick  
1634 line is median, whiskers are most extreme data points not considered outliers, see  
1635 Methods. **g**, Histogram of the difference between correlated and anti-correlated odour  
1636 responses. Box plots as in **f**. **h**, Comparison of correlated and anti-correlated odour  
1637 responses of all dendritic ROIs ( $f = 20$  Hz,  $n = 514$  dendrites). **i**, Classifier accuracy when  
1638 trained on all dendritic ROIs recorded with a sliding window of different durations  
1639 starting 2 seconds before odour onset (colour-coded, black: shuffle control,  $n = 514$  from  
1640 6 individual animals; mean  $\pm$  SD, 100 repetitions). **j-m**, same as **f-i** for projection neuron  
1641 somata ( $f = 20$  Hz,  $n = 680$  cells; see Fig. 3).

1642 **Extended Data Fig. 8 | Projection neurons unit recordings in response to correlated**  
1643 **vs. anti-correlated stimulation and short odour pulse combinations.**  
1644 **a**, Data from unit recordings as described in Fig. 3h-k. Average waveforms across all  
1645 channels of two isolated units shown in **b<sub>i,ii</sub>**. Each waveform represents the average  
1646 waveform for the unit on a specific channel. Red waveform indicates the channel with the  
1647 largest average waveform for the unit. Scale bar in the bottom left represents 100  $\mu$ V  
1648 (vertically) and 1 ms (horizontally). **b**, Additional example single unit odour responses to  
1649 correlated (black) and anti-correlated (red) stimuli shown as raster plot (top) and PSTH  
1650 (mean of 64 trials for each condition  $\pm$  SEM) of spike times before (second from top) and  
1651 after baseline subtraction (second to bottom), and the differential PSTH of correlated and  
1652 anti-correlated (bottom, blue). Average spike waveform shown as insets in **b<sub>i,ii</sub>**. Duration  
1653 of odour presentation (2 s) is indicated in light blue. P-values are derived from a two-  
1654 sided Mann-Whitney U test comparing the spike time distributions of correlated and anti-  
1655 correlated trials during 4 s after odour onset. **c**, Average baseline firing rate for all units  
1656 ( $n = 97$  from 6 individual animals). Baseline firing rates were calculated from 4 s to 0 s  
1657 before odour onset for each of the 1312 trials presented during all recordings. Violin plot  
1658 shows the median as a black dot and the first and third quartile by the bounds of the black  
1659 bar. **d<sub>i</sub>**, Classifier accuracy when trained on all baseline-subtracted units in response to  
1660 20 Hz correlated vs. anti-correlated stimulation ( $n = 97$  units, mean  $\pm$  SD from 6 individual  
1661 animals) with a sliding window of different durations (colour-coded; black: shuffle  
1662 control; 100 repetitions) starting at 2 s before odour onset. Time along the x-axis  
1663 represents the end time of the window. **d<sub>ii</sub>**, Time period between -0.5 and 0.5 s from  
1664 odour onset shown at higher magnification ( $n = 97$  units, mean  $\pm$  SD from 6 individual  
1665 animals). **e**, To take the entire temporal structure of responses into account we  
1666 performed a principal component analysis (PCA) on the temporal evolution of the firing  
1667 rate responses (see Methods). Shown here is the accuracy for linear SVM classifiers  
1668 (mean  $\pm$  SD) trained on increasing numbers of principal components (PCs). Classifiers  
1669 were trained on all but two trials (one correlated, one anti-correlated). Training and  
1670 testing were repeated 1000 times. The colour code represents the same window sizes as  
1671 defined in **d**. **f**, The first (**f<sub>i</sub>**), second (**f<sub>ii</sub>**), and third (**f<sub>iii</sub>**) PCs found from PCA for different  
1672 rolling window sizes (colour code as defined in **d**). In the second and third PCs, the

1673 windows have been split as to better compare the similarities in PCs for different window  
1674 sizes. **g**, Average classifier accuracy of a set of classifiers trained on the PC weights of  
1675 increasing number of units. Classifiers were trained on all but two trials (one correlated,  
1676 one anti-correlated). The number of PCs used for each window was selected by the peak  
1677 accuracies in **e** (colour-coded;  $n =$  up to 97 units from 6 individual animals; mean  $\pm$  SD of  
1678 1000 classifier repetitions). **h**, Schematic of odour pulse stimuli timings in relation to the  
1679 respiration cycle. Three combinations were presented, each trial 120 ms in length. For  
1680 example, 11000 (top) consisted of a 40 ms odour pulse (light blue) followed by 80 ms of  
1681 blank odourless air (grey); All trials were triggered at the onset of inhalation. **i**, PSTH from  
1682 four example units (**i**-**iv**) showing their average firing rate prior, during, and after odour  
1683 presentation (light blue vertical bar). Responses are either to 11000 trial (black) or  
1684 10100 odour presentation (red). The instantaneous firing rate was calculated by  
1685 summing the number of detected spikes in 10 ms windows and multiplying the value by  
1686 100 to get Hz. **j**, Accuracy of linear classifiers as a function of the number of units available  
1687 for training/testing (mean  $\pm$  SD of  $n =$  up to 145 units from 8 individual anaesthetised  
1688 animals). Each classifier is trained on the summed spike count of the available units in a  
1689 window of 500 ms starting at odour onset. The classifiers were trained on all but two  
1690 trials, one 11000 and one 10100 trial and the number of repeats between animals varied  
1691 between 11 and 30. To account for this and to minimise the variability of the training set,  
1692 trial number was bootstrapped to 1000 repeats. This was achieved by randomly selecting  
1693 a repetition for each unit independently. The test set was isolated from the responses  
1694 prior to bootstrapping and thus was not seen by the classifier until it was tested on it.  
1695 Each classification was repeated 500 times with a different selection of units, and a  
1696 different test set. The shuffled control (black) was accomplished by shuffling the training  
1697 labels during each iteration of the classifier without shuffling test labels. **k**, Same as in **j**  
1698 but classifying all three odour pulse combinations shown in **h**. **l**, Confusion matrix  
1699 showing the fractions that each trial type was classified as ( $n = 145$  units from 8  
1700 individual animals). True labels are shown on the x-axis and labels predicted by the  
1701 classifier on the y-axis. Accuracies correspond to maximum unit count shown in **c** and **d**.  
1702 The classifiers can readily separate between trials containing a single 40 ms odour pulse.  
1703 Accuracy is lower when distinguishing between an intermission of 20 or 40 ms but  
1704 remains above chance (chance = 0.33).

1705 **Extended Data Fig. 9 | Whole cell recordings of projection neurons in response to**  
1706 **correlated vs. anti-correlated odour stimulation.** **a**, Schematic of the whole-cell patch  
1707 clamp recording approach. **b**, Distribution of input resistance and **c**, recording depth as  
1708 measured from all recorded projection neurons ( $n = 31$ ). **d**, Left: Example recording from  
1709 single cells with consecutive presentations of correlated (black) and anti-correlated (red)  
1710 odour stimulus at 2 Hz. Duration of odour presentation (2 s) is indicated in light blue.  
1711 Right: Baseline-subtracted and spike-clipped subthreshold voltage response from a  
1712 single cell to odour 1 (green) and odour 2 (blue) for 2 Hz. **e**, the same as **d** but for 20 Hz  
1713 odour stimulation. **f**, Voltage response from three example cells for correlated (black) and  
1714 anti-correlated (red) odour stimulus for 2 Hz (top) and 20 Hz (bottom). The cell shown  
1715 in **f** corresponds to the cell shown in **d** and **e**. The grey overlaid traces correspond to the  
1716 arithmetic sum estimated from the response to individual odours. Bottom: Linear  
1717 prediction histogram calculated by thresholding the arithmetic sum of the subthreshold

1718 responses to the individual odours. Differences here suggest that correlation can be  
1719 calculated based on a single cell level if the two individual odours engage overlapping  
1720 OSN populations. P-values are derived from a paired two-sided t-test of the membrane  
1721 potential and the firing rate in the first 500 ms after odour onset. **g**, Average change in  
1722 voltage (**g<sub>i</sub>**) and in instantaneous spike frequency (**g<sub>ii</sub>**) in the first 500 ms after odour  
1723 onset from baseline membrane potential for 2 Hz correlated vs. anti-correlated odour  
1724 presentation and **h**, for 20 Hz. Each marker corresponds to a single cell, error bars  
1725 represent SEM. Data points in black represent cells where  $p < 0.05$  between correlated  
1726 and anti-correlated conditions. P-values are derived from a paired t-test of the membrane  
1727 potential and the firing rate in the first 500 ms after odour onset. Indicators (i), (ii) & (iii)  
1728 represent cells shown in **f**. **i**, Pie charts depicting the proportion of cells showing  
1729 significant difference as described above (blue) in subthreshold membrane potential  
1730 (left) and spike frequency (right) for all 2Hz (top) and 20Hz (bottom) cells. P-values are  
1731 derived from a paired t-test of the membrane potential and the firing rate in the first 500  
1732 ms after odour onset.

1733 **Extended Data Fig. 10 | Odour plume generation and additional analysis of source**  
1734 **separation experiments.** **a**, Power spectrum of all recorded odour plumes (mean  $\pm$  SD  
1735 of log power,  $n = 132$  plumes). **b**, Cross correlation of all recordings at different lateral  
1736 separation distances. **c**, Correlation coefficients over all recordings for odours from the  
1737 same source and for odour sources separated by 50 cm in a controlled laboratory  
1738 environment with complex airflow (indoors; ethyl valerate (EV) vs. tripropylamine  
1739 (TPA);  $n = 25$  for same source,  $n = 27$  for sources separated by 50 cm;  $p < 0.0001$ , unpaired  
1740 two-sided t-test). Box indicates 25<sup>th</sup> – 75<sup>th</sup> percentiles, thick line is median, whiskers are  
1741 most extreme data points not considered outliers; see Methods. **d**, Same as Figure 4b (for  
1742 odours  $\alpha$ -Terpinene and ethyl butyrate) but for radial distances to the PID of 20 cm and  
1743 60 cm ( $p < 0.0001$ , unpaired two-sided t-test). **e**, Same as **d** but measured outdoors ( $n =$   
1744 7 for same source, 10 for sources separated by 50 cm;  $p < 0.001$ , unpaired t-test; Indoors  
1745 versus outdoors, one source:  $p = 0.0060$ ,  $s = 50$  cm:  $p = 0.0632$ , unpaired two-sided t-  
1746 test). **f**, Example plume structures originating from the same one source or separated  
1747 sources as recorded with a PID (blue) and replayed with the multi-channel high  
1748 bandwidth odour delivery device (orange). **g**, Correlation coefficients over all recordings  
1749 of replayed plumes for one source ( $n = 53$  plumes) and for sources separated by 50 cm  
1750 from each other ( $n = 74$  plumes;  $p = 2.27e-41$ , unpaired two-sided t-test). **h**, Odour signals  
1751 integrated over 2 s for all recordings of replayed plumes for one source ( $n = 53$  plumes)  
1752 and for sources separated by 50 cm ( $n = 74$  plumes;  $p = 0.75$ , unpaired two-sided t-test).  
1753 **i**, Odour plume signals integrated over 2 s for rewarded and unrewarded trials ( $n = 150$   
1754 trials each; Odour 1:  $p = 0.4739$ , Odour 2:  $p = 0.0923$ , unpaired two-sided t-test). **j**,  
1755 Overlaid power spectra (mean  $\pm$  SD of log power) of all plumes ( $n = 127$  plumes) recorded  
1756 in complex, natural airflow conditions (blue) and replayed plumes (orange). **k**, Schematic  
1757 of plume reproduction: First, a 2s long window is selected from the PID recording,  
1758 starting around the middle of the trace and such that odour is present during the first 500  
1759 ms. Secondly, the trace is normalised between 0 and 1. Thirdly, the trace is converted into  
1760 a series of binary opening and closing commands directly related to the value of the

normalised signal. A value of 1 translates to a continuous opening, and a value of 0 translates to continuously closed. This series of commands is relayed to an odour valve and an inverted version of the commands is relayed to a mineral oil valve to generate a compensatory airflow. The resulting output resembles the original plume, as measured with a PID, and there is constant airflow throughout the trial, as measured with a flow meter. The same procedure is then applied to the accompanying odour, to create both plumes needed for each trial. **I**, Group learning curves (mean  $\pm$  SD) for the two groups of animals trained on the virtual source separation task, but on different set of valves. Group 1 ( $n = 6$  mice, blue) were trained on the task from the start, while Group 2 ( $n = 6$  mice, cyan) were first exposed to a scrambled version of the task and were later transferred to the same plumes as Group 1. This served as a control that the cue required for learning is indeed olfactory information contained in the odour plumes. For the 3<sup>rd</sup> stage of learning, the plumes were refined to ensure odour was always present in the first 500 ms of the trial and performance stabilised for the two groups. Mice progressed through these learning stages as a group, based on time elapsed from the beginning of training. Therefore, some mice performed more trials than others. The last trial performed by a mouse in each phase is represented by a colour-coded circle above the plot. Accuracy is calculated over a 100-trial sliding window. **m**, Rejection fraction (fraction of trials the mouse abstained from licking) calculated for each plume pair plotted in relation to the correlation between the two odour traces in that plume pair. Animals are trained to lick (expected low rejection fraction) for source separated trials (low correlation) and abstain from licking (high rejection fraction) for one source trials (high correlation). **n**, Difference in lick rates in response to source separation training trials ( $n = 9$  mice, mean  $\pm$  SD), calculated for each mouse as lick rate (licks / 100 ms) in response to S+ trials minus the lick rate in response to S- trials, normalized to averaged lick rate for all trials across the corresponding time period. **o**, Reaction times for each mouse, calculated as the time point when the difference in lick rate for each mouse crossed a threshold (mean + 3 SDs over the baseline, defined as the first 200 ms of the trace, when odour was not present). Box indicates 25<sup>th</sup> – 75<sup>th</sup> percentiles, thick line is median, see Methods. **p**, Trial map of all animals during virtual source separation tasks before and after introduction of control valves similar to Extended Data Fig. 4 ( $n = 40$  trials pre-,  $n = 40$  trials post-new valve introduction, new valve introduction indicated by black vertical line). Each row corresponds to an animal, each column within the row represents a trial. Light green: hit, dark green: correct rejection, light red: false alarm, dark red: miss. **q**, Mean performance of animals ( $n = 11$  mice) that reached performance criterion during training during pre- and post-control. **r**, Discrimination accuracy split by stimulus valence (green, S+; black, S-) for odour correlation fluctuation frequencies 2, 20 and 40 Hz (Fig. 4e;  $n = 9$  mice, data is mean  $\pm$  SD, unpaired two-sided t-test). **s**, Group performance for the square pulse probe trials at different frequencies, in animals trained on the source separation task (blue dots,  $n = 9$  mice, data is mean  $\pm$  SD), compared to group performance where animals were trained on correlated and anti-correlated square pulse trains (from Fig. 2k, black line and SEM band,  $n = 33$  mice; 2 Hz:  $p = 0.0018$ , 20 Hz:  $p = 0.19$ , 40Hz:  $p = 0.94$ , unpaired two-

1803 sided t-test). Violin plots in **g-i** show the median as a black dot and the first and third  
1804 quartile by the bounds of the black bar.

1 **Supplementary Information Guide**

2 **Supplementary Video 1:** Automated operant conditioning system ("AutonoMouse")  
3 equipped with high speed odour delivery device.

4 **Supplementary Video 2:** Comparison between original video-based respiration  
5 recording and phase-based motion amplification (red trace) in head-fixed condition on  
6 the animal's flank to capture body movements associated with respiration.  
7 Simultaneously, respiration was recorded with a flow sensor placed in front of one nostril  
8 (black trace). Odour stimulus highlighted with blue bar.

9 **Supplementary Methods Fig. 1 | Characterization of odorants presented with a**  
10 **high-speed odour delivery device.** **a**, Calculated signal fidelities for seven different  
11 odours (colours, see legend in **b**) pulsed for 2 s over a frequency range of 2 to 100 Hz at  
12 50% pulse duty ( $n = 5$  repeats for each condition, mean  $\pm$  SEM). **b**, Amount of released  
13 odour ( $n = 5$  repeats for each condition, mean  $\pm$  SEM). Odours are: AA (isoamyl acetate),  
14 ACP (acetophenone), AT ( $\alpha$ -Terpinene), CN (cineol), EB (ethyl butyrate), Hex (2-  
15 hexanone), PEA (phenylethyl alcohol). **c**, Left: Schematic of the pulse-width modulation  
16 (PWM) method. For any period of odour release, maximum final concentration is  
17 achieved by keeping the valve open for the entire time (top). The amount of odour  
18 released can be reduced by cycling the valve at a high frequency (here 500 Hz) with a  
19 different level of PWM (middle and bottom panel). Right: Odours were released over a 2  
20 s period with different PWM duties at 500 Hz ( $n = 5$  repeats for each condition, mean  $\pm$   
21 SEM). The resulting amount of released odour is normalised to the maximum release  
22 (PWM = 1). **d**, Average PID signal of single 100 ms pulses (pulse indicated in blue) for  
23 seven different odours ( $n = 60$  pulses for each odour, mean  $\pm$  SEM). **e**, Summary table:  
24 delay (time from start of the odour pulse to 5% of maximum signal amplitude), rise (time  
25 from 5% to 95% of maximum signal amplitude), decay (time for the signal to decay back  
26 to 5% of maximum amplitude after the end of the odour pulse). **f**, Effect of tubing length  
27 attached to the valve manifold on signal fidelity at different pulse frequencies pulsed for  
28 2 s at 50% pulse duty (ethyl butyrate).

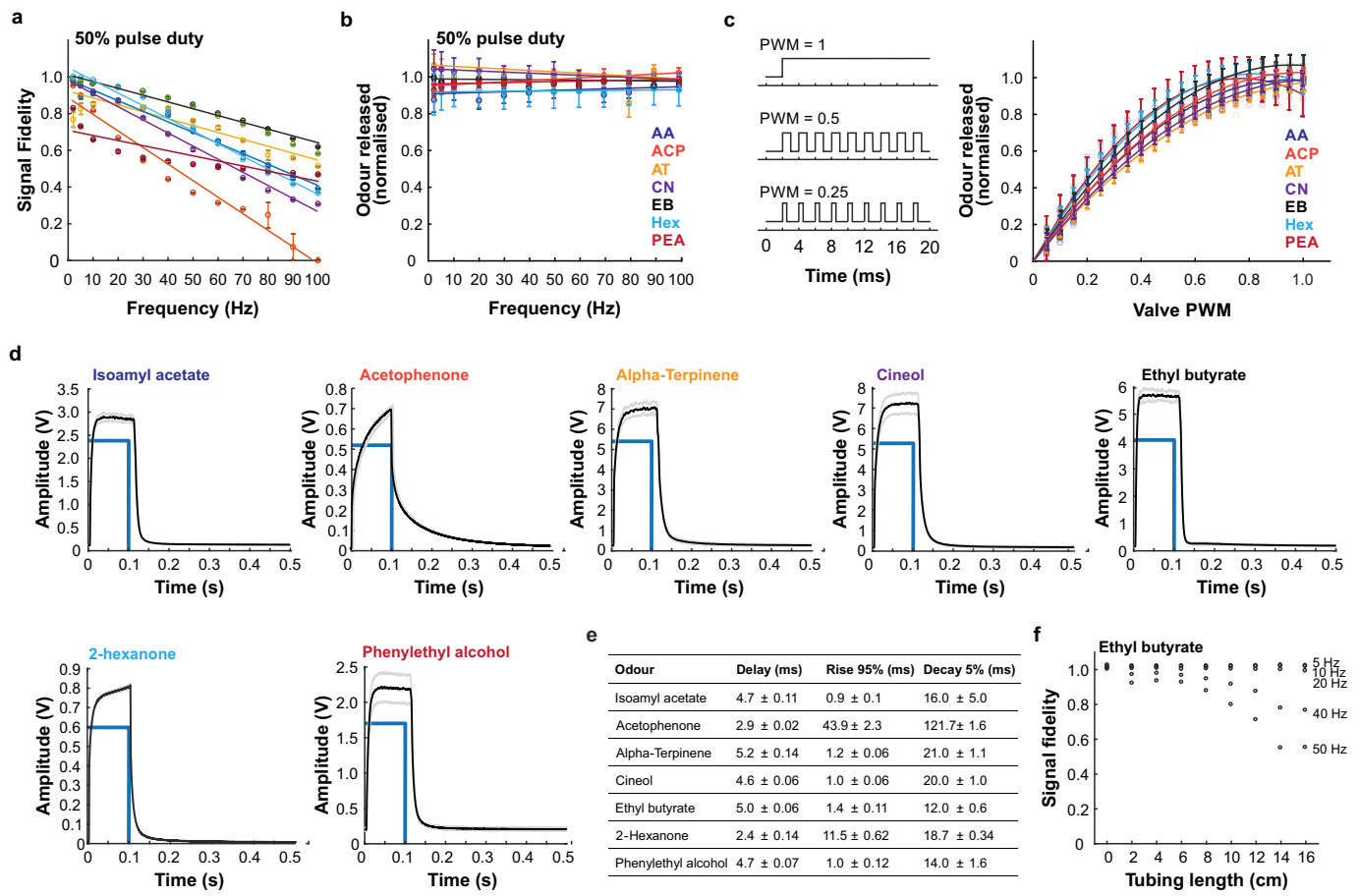
29 **Supplementary Methods Fig. 2 | Dual-energy fast photoionisation detection**  
30 **(defPID).**

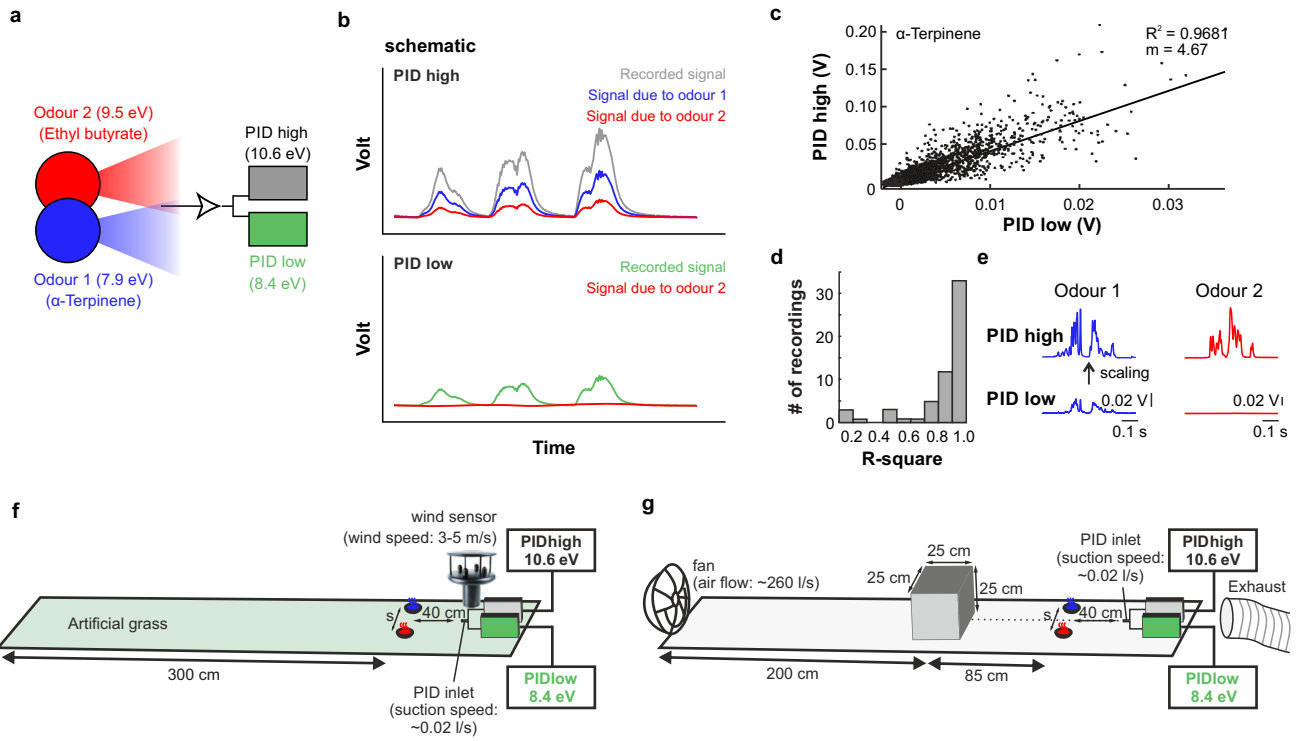
31 **a**, Schematic of the dual-energy fast photoionisation detection method. Two odours are  
32 recorded simultaneously by two PIDs with different ionizing energies (different  
33 wavelength UV light sources). The odours are chosen such that one odour (odour 2 (ethyl  
34 butyrate), 9.5 eV) has an ionization energy greater than the low energy PID bulb, but less  
35 than the high energy PID bulb, thus only being detectable by the high energy PID. The  
36 other odour (odour 1 ( $\alpha$ -Terpinene), 7.9 eV) is chosen such that its ionization energy is  
37 lower than both PID bulbs (detectable by both PIDs, see also **e**). **b**, Method of  
38 decomposing odour signals. Top panel: high energy PID signal (grey: recorded signal,  
39 blue: calculated signal due to odour 1, red: calculated signal due to odour 2). Bottom  
40 panel: low energy PID signal (green: recorded signal, red: calculated signal due to odour  
41 2; the entire signal is due to odour 1). **c**, Single data points of the PID signal evoked by  $\alpha$ -  
42 Terpinene in the two PIDs. The slope of the linear fit serves as a scaling factor to map the  
43 low energy PID to the high energy PID signal. **d**, Histogram of R-squared values of all dual-

44 PID  $\alpha$ -Terpinene recordings to define the scaling factor (n = 59 recordings). **e**, Summary  
45 of signal combinations for defPID recordings. The scaling factor for the PIDlow signal is  
46 determined by the slope in **c**. **f**, Schematic of outdoors odour plume recording setup. PIDs  
47 and odour delivery system were used to record for multiple trials at different lateral  
48 distances (s) between odours held in ceramic crucibles. Data was collected on a day with  
49 low wind (~8-12 mph, equivalent to ~3-5 m/s, recorded with a 2-axis ultrasonic wind  
50 sensor at the height of the PID inlet. Outdoor experiments were performed on a ~6 m x  
51 10 m wooden patio structure surrounded by trees. There was >300 cm of unobstructed  
52 space on an artificial grass mat in front of the PIDs to capture air movements. **g**, Indoor  
53 setup: A digitally controlled fan was placed at a distance of 325 cm facing the PID inlet.  
54 An exhaust line was situated behind the PID inlet to ensure the direction of air from the  
55 fan towards the PID inlet. During a recording, the fan was set to maximum speed such  
56 that it pushed approximately 552 cf/min (cubic feet per minute, ~260 l/s) of air towards  
57 the PID inlet. A 25x25x25 cm Thermocool box was placed 200 cm downwind of the fan  
58 acting as an obstacle to air movement, promoting complex air movement patterns at the  
59 PID location. The pump at the PID was set to ~0.02 l/s suction speed, unlikely to perturb  
60 overall airflow dynamics substantially.

61 **Supplementary Table 1:** Parameters of the olfactory sensory neuron population model.

62 **Supplementary Table 2:** Parameters of the olfactory sensory neuron population model  
63 that were varied.





**Supplementary Table 1: Parameters of the olfactory sensory neuron population model**

Parameter	Description	Value
$\tau_C$	Olfactory transduction time constant	75 ms
$\tau_V$	OSN membrane time constant	75 ms
$\sigma$	Standard deviation of OSN membrane voltage additive noise	0.25 V
$a$	Stimulus amplitude	15 V
$\theta$	OSN spike threshold	2 V
$t_{ref}$	OSN refractory period	1 sec
$V_{ref}$	OSN refractory voltage	-1 V
$\tau_h$	Ca2+ imaging filter time constant	150 ms
$\Delta t$	Euler integration step size	1 ms

**Supplementary Table 2: Parameters of the olfactory sensory neuron population model that were varied**

Parameter	Centre	Minimum	Maximum
$\tau_V$	75 ms	56.25 ms	93.75 ms
$\tau_C$	75 ms	56.26 ms	93.75 ms
$\sigma$	0.25 V	0.1875 V	0.3125 V
$\theta$	2 V	1.5 V	2.5 V
$a$	5	3.75 V	6.25 V